LUND UNIVERSITY
Faculty of Science

Studies of Possible QGP Estimators in proton-proton Collisions

Anna Önnerstad

Thesis submitted for the degree of Master in Particle Physics
Project duration: 10 months

Supervised by Peter Christiansen

Department of Physics
Division of Particle Physics
May, 2019

Abstract

This thesis presents studies of three different Quark-Gluon Plasma estimators in proton-proton collisions using what is currently believed to be quark-gluon plasma observables; radial flow, elliptic flow and strangeness enhancement. The three tested estimators were Transverse Spherocity, an altered version of Transverse Spherocity where all p_T was put to one, and a newly developed estimator called Mid-Forward. The first part involved simulation studies where the estimators were tested using different settings within the Rope Hadronization framework in PYTHIA. The aim for this thesis was to find an estimator working for all three observables. However, this was not achieved as the results from the simulation study indicated that both spherocity estimators work well for the radial flow observable but not for elliptic flow, while the mid-forward estimator did not perform well for radial flow, it was the best candidate when measuring elliptic flow. Therefore the mid-forward estimator was selected for the data analysis of elliptic flow using two particle correlations. These results did not agree with what was observed in the results from the simulation studies, which could be due to low statistics in the data analysis.

Populärvetenskaplig Sammanfattning

Forskning inom partikelfysik grundar sig i att försöka förstå naturens lagar vilket har givit oss insikt i den fundamentala strukturen av materia. Man trodde länge att atomen var den minsta byggsten av materian runt omkring oss (där atom kommer från grekiskans átomos och betyder odelbar), men forskning visade att detta inte stämde. En förenklad modell är att atomen består av elektroner som kretsar runt en atomkärna, där kärnan kan delas upp i atomer och neutroner som i sin tur består av kvarkar och gluoner.

Vår nuvarande kunskap om den fundamentala strukturen av materia är samlad i den så kallade Standard Modellen av partikelfysik som ger en matematisk beskrivning av elementarpartiklar och deras växelverkan. Elementarpartiklarna som ingår i Standard Modellen delas in i två grupper; fermioner och bosoner, där fermioner är de partiklar som utgör all materia och bosoner är de kraft-förmedlande partiklarna som växelverkar mellan fermionerna. I Standard Modellen ingår även tre fundamentala krafter; den starka, den svaga och den elektromagnetiska kraften. Den starka kraften är, som kanske förstås av namnet, den starkaste av de tre krafterna och är den som håller ihop elementarpartiklarna och då bildar större partiklar som kallas hadroner. Exempel på hadroner är protonen och neutronen.

Bosonen som förmedlar den starka kraften kallas gluon och har, till skillnad från fotonen som är den kraft-förmedlande bosonen för den elektromagnetiska kraften, inte bara en elektrisk laddning utan även färgladdning. Även kvarkar har färgladdning. Gluonens färgladdning medför att gluonen kan växelverka med sig själv som i sin tur ger upphov till att kvarkar inte kan existera fritt utan att de alltid är sammansatta i färg-neutrala hadroner.

Det har dock länge funnits teorier om att vid extremt höga temperaturer och/eller partikel densiteter så “smälter” hadronerna till ett tillstånd där kvarkar och gluoner är nästan fria. Detta tillstånd kallas Kvark-Gluon Plasma, och man tror att denna plasma existerade under de första micro-sekunderna efter Big-Bang när Universum var extremt varmt och hade hög täthet. Man tror även att plasman idag existerar i kärnan av neutronstjärnor på grund av den höga densiteten där.

Idag kan de höga temperatur - och densitet - tillstånden som krävs för att skapa plasman uppnås i laboratoriemiljö med hjälp av partikelacceleratorer där man kan kollidera tunga joner i höga energier. Ett exempel på ett sådant experiment är ALICE experimentet som är ett av fyra experiment vid LHC (Large Hadron Collider) på CERN i Genève. Där har man lyckats att komma upp i en temperatur på ca 740 MeV vilket motsvarar 1.5 miljarder gånger varmare än solens yta.

Plasman som skapas i laboratoriemiljö har en livstid på endast 10^{-22} sekunder innan kvarkarna och gluonerna förenas och bildar hadroner igen. Denna korta livstid gör det omöjligt att direkt studera plasman och man får därför studera olika karaktäristiska signaturer av de partiklar (hadroner) som man kan detektera. Man har länge trott att plasman endast kan skapas vi energi-densiteten som uppnås vid tung-jons kollisioner, dvs kollisioner mellan t.ex. bly eller guld joner, men detta har man nyligen börjat ifrågasätta då man observerat kvark-gluon plasma signaturer vid kollisioner mellan proton och bly, och proton-proton. För att undersöka detta behövs inte bara mer data (mer statistik) utan även nya typer av mätningar som är känsligare för den underliggande fysiken. Ett exempel på en sådan mätning som används nu är Transverse Spherocity. Den delar upp proton-proton kollisioner i olika kategorier beroende på kollisions formen i det transversa planet. Det har dock nyligen visat sig att Transverse Spherocity fungerar bra för några plasma signaturer så som radial flow, men att den kanske inte alls fungerar för andra signaturer så som elliptic flow. Mål för denna uppsatsen är därför att komma på och testa alternativa mätningsmetoder för kvark-gluon plasman.

Det första steget var att testa och utveckla de nya ideerna på simulerad data med olika modeller för att utifrån det välja ut några signaturer och metoder och testa dem på data från ALICE för att se hur metoderna fungerar för de olika signaturerna. Om någon utav metoderna skulle fungera för de olika plasma signaturerna så hade det kunnat leda till en bättre förståelse av de kollektiva effekter som man har observerat i de mindre kollisions systemen. Om det även visar sig att dessa effekter beror på ett medium som expanderar har skapats i de små systemen (så som i de större tung-jons systemen) så kan detta innebära att de större systemen kan tolkas som en förlängning av de små systemen. Dessa slutsatser hade varit banbrytande och betytt att man hade fått tänka om när det kommer till vår kunskap om den starka kraften och tung-jons fysiken.

Acknowledgments

I want to give a big thank you to my supervisor Peter Christiansen for giving me the opportunity to work on this project and for always being a positive support. I would also like to thank David Silvermyr for taking his time to help me with my programming issues and Anders Oskarsson for proof reading this thesis and for being someone to ask for advice. Then we have the Lund ALICE office; Adrian Nassirpour, Jonatan Adolfsson, Oliver Matonoha, Omar Vazquez, Lisa Vergara and Martin Angelsmark... thank you so very much for everything, you are the absolute best!! A special thank you to Lisa, without you I would never have made it this far in my education. Lastly I would like to thank the Lund Particle Physics division, it has been a huge inspiration to be around such amazing and smart people with the biggest hearts.

Contents

1 Introduction

In the field of particle physics, the aim is to understand the laws of nature by studying the fundamental building blocks of matter and their interactions. Our current understanding is embodied in a mathematical theory called the Standard Model of particle Physics, which provides a description of these fundamental particles and the forces between them [1]. A quark is one of the elementary particles in the Standard Model. In stable matter, quarks are bound together into protons and neutrons by the force mediating particles of the strong interaction, called gluons. The protons and neutrons together with electrons will in turn form atoms that constitute all matter in the Universe in the form of solids, liquids and gases.

Due to the concept of confinement arising from the strong force, no free quarks or gluons have been observed. However, the theory of the strong interaction, Quantum Chromodynamics, predicts that a phase transition from ordinary matter into a state where quarks and gluons are deconfined will occur, and that this could be achieved by colliding heavy-ions at high energies. This deconfined state of matter is called Quark-Gluon Plasma and is believed to have existed $\sim 10\ \mu s$ after the Big Bang.

As the theory predicted, Quark-Gluon Plasma has been created by colliding heavy ions, such as lead or gold. It is, however, not possible to directly observe the plasma because of the short life-time ($\sim 10^{-22}$ s) when created in the laboratory. Instead it reveals itself through observable signatures by analysing the detected final-state particles.

1.1 Motivation for This Thesis

Up until recently it was believed that the energy-density needed to produce Guark-Gluon Plasma could only be done through heavy-ion collisions such as lead-lead (Pb-Pb) or gold-gold (Au-Au), but this has been questioned since plasma-like signatures have been observed in proton-lead (p-Pb) and proton-proton (pp) collisions. The plasma signatures are hard to observe in these small systems due to the dominating hard scattering effects. For this reason, quark-gluon plasma estimators are used as a tool to isolate soft, plasma physics from hard physics in hopes of making it easier to study the plasma effects. One such estimator is the Transverse Spherocity estimator, which divides events into soft and hard physics depending on their event shapes. Transverse Spherocity has proven to work well for the radial flow observable, however it does not work at all for other observables, one of them being the elliptic flow giving rise to a double ridge.

In Ref.[2] an attempt to isolate a double ridge by using a data set of pp collisions at $\sqrt{s} = 13$ TeV was done by utilizing multiplicity and transverse spherocity, where the results displayed potential issues with the transverse spherocity estimator. When dividing the collisions into high multiplicity jetty and isotropic events, the angular pair-correlation distribution looked as if there were some kind of bias on the ϕ-distribution for the selected isotropic events. Hence, the first step in this analysis was to see if Monte Carlo simulations showed the same phenomena, and if it did, new estimators had to be developed and tested on different observables and data sets. The goal is to find an estimator that works well for all guark-gluon plasma observables.

The Standard Model and some phenomenology of high-energy physics is introduced in chapter 2. In chapter 3, a description of the quark-gluon plasma is given together with its observables and the ideas behind the Lund string model. A brief overview of the ALICE detector is given in chapter 4. In chapter 5 the analysis performed in this project is described, followed by the results and discussion in chapter 6. Finally, conclusions made from this work and an outlook is presented in chapter 7.

2 Introduction to High-Energy Physics

2.1 The Standard Model

The Standard Model (SM) of particle physics attempts to describe the fundamental structure of matter. It is a Quantum Field Theory (QFT) that provides a mathematical description of the properties and interactions of two types of elementary particles[1]; *fermions* with half-integer spins and *bosons* with integer spins [3]. The different type of particles will be further discussed in Section 2.1.1. These elementary particles are treated as excited states of their corresponding underlying quantum fields, and interact by exchanging field quanta in the form of force mediating particles. An example of this is electromagnetic interactions that is described by Quantum Electrodynamics (QED) [4]. QED is a QFT where the electromagnetic interaction is mediated by a boson called the photon and acts on charged fermions, e.g. electrons, where an electron would be a representation of a quantum state of a fermion field, while the photon would be a quantum state of an electromagnetic field. The Standard Model is often presented in the form of a table with all the elementary particles and their properties. This table is based on a mathematical formulation of the SM referred to as the SM Lagrangian.

2.1.1 Fundamental Particles and Forces

In total there are 17 elementary particles within the SM framework; 12 fermions and five bosons, that all have different quantum numbers. One of these quantum numbers is spin which is associated with the particle's intrinsic angular momentum. The particles could have either half-integer spin or integer (0 included) spin. Particles with half-integer spin are called fermions and particles with integer spin are called bosons.

Fermions are the elementary building blocks of matter and they interact with the exchange of bosons. All fermions are divided up into three generations. The particles in the second and third generations have the same properties as the particles in the first generation but with an increase of mass for each generation.

The spin-1/2 fermions obey the Pauli exclusion principle [6], which states that no two identical fermions (fermions with identical quantum numbers) can occupy the same quantum state at the same time. This means that at least one property has to be different. The dynamics (including spin) of the fermions is described by the relativistic Dirac equation. Another important consequence from the Dirac equation is that it follows from its solutions that for every fermion there exists an antiparticle with exactly the same mass but with an opposite electrical charge. These antiparticles are usually denoted by their charge or by a bar over the particle symbol [1].

Fermions are divided into two subgroups, six quarks and six leptons, depending on which force they experience. All twelve fermions can interact weakly, and all electrically charged fermions can interact electromagnetically, i.e. all fermions except for the electrically neutral neutrinos. Quarks carry an extra quantum number called color-charge, the strong force equivalent to the electric charge, and are therefore the only fermions

---

[1] Elementary particles are treated as point-like particles with no known internal structure or excited states [3].

Table 1: The 12 elementary fermions in the Standard Model. The particles are presented together with their masses and charges (Q) given by the Particle Data Group [5]

Fermions (Spin 1/2)						
Generation	**Quarks**			**Leptons**		
	Particle	**Mass**	**Q**	**Particle**	**Mass**	**Q**
I	Up (u)	2.2 MeV	$+\frac{2}{3}\ e$	Electron Neutrino (ν_e)	$<$ 2.2 eV	0
	Down (d)	4.7 MeV	$-\frac{1}{3}\ e$	Electron (e)	0.5 MeV	-1 e
II	Charm (c)	1.28 GeV	$+\frac{2}{3}\ e$	Muon Neutrino (ν_μ)	$<$ 170 eV	0
	Strange (s)	95 MeV	$-\frac{1}{3}\ e$	Muon (μ)	106 MeV	-1 e
III	Top (t)	173 GeV	$+\frac{2}{3}\ e$	Tau Neutrino (ν_τ)	$<$ 11.5 MeV	0
	Bottom (b)	4.18 GeV	$-\frac{1}{3}$ e	Tau (τ)	1.78 MeV	-1 e

that interact strongly. The six leptons are the electron, muon, tau-lepton and the their neutrinos. All the different types (flavors) of fermions and their properties are presented in Table 1.

There are four fundamental forces; the strong force, the electromagnetic force, the weak force and the gravitational force, although only the former three are included in the SM since there is not yet a complete QFT for gravity. However, the effect of the gravitational force between the miniscule elementary particles is so small that it can be neglected. The forces included in the SM are all mediated by spin-1 gauge bosons. Because they have integer spin, bosons do not have to obey the Pauli exclusion principle and can therefore occupy the same quantum state.

It appears that most stable matter is formed from just the first generation of fermions. An atom is made up of one negatively charged electron that orbits a positively charged nucleus that is composed of two kind of hadrons, namely protons (two up quarks and one down quark) and neutrons (one up quark and two down quarks). The electron and the nucleus are bound together by the electromagnetic force described by QED and is mediated by the massless gauge boson called the photon that acts on electrically charged particles. Another well-known fermion from the first generation is the electron neutrino which is observed in the decay products of neutron β-decay [3]. The force associated with this decay is the weak charge-current interaction that is mediated by the massive electri-

Table 2: The four elementary bosons of the Standard Model. The particles are presented together with their charge (Q), mass and strength given by the Particle Data Group [5].

Bosons (Spin 1)					
Force	**Mediator**	**Q**	**Mass**	**Strength**	**Acts on**
Strong	Gluon (g)	0	0	1	Color charged particles
Electromagnetic	Photon (γ)	0	0	10^{-3}	Electrically charged particles
Weak	$W^{\pm}$	$\pm 1\ e$	80.4 GeV	10^{-8}	Fermions, electroweak gauge bosons
	Z^0	0	91.2 GeV		

cally charged $W^{\pm}$ bosons. There is also the weak neutral-current interaction mediated by the massive electrically neutral Z^0 boson. The weak charge-current and neutral-current interactions are together referred to as just weak interactions. These are the only interactions that allow fermions to change flavor [1]. The quarks in the proton and neutron are bound together by the strong force which is mediated by eight massless gauge bosons called gluons that only couple to color charges. The strong force is described by the QFT called Quantum Chromodynamics (QCD) and will be discussed in more detail in section 2.2.

In 2012 the ATLAS and CMS experiment at the Large Hadron Collider discovered the massive Higgs boson, H^0, which is the newest elementary particle in the SM. Unlike the other gauge bosons with spin-1, the H^0 is a spin-0 scalar boson [1]. It is assumed that the Universe is filled with a Higgs field that generates mass to the fermions and weak bosons through the Higgs mechanism; an electroweak symmetry breaking of the SU(2) and U(1) groups [7], which is an important role for the SM and explains why the $W^{\pm}$ and Z^0 acquire mass while the photon does not.

2.2 Quantum Chromodynamics

As mentioned in section 2.1.1 Quantum Chromodynamics is the QFT that describes the short ranged strong force in the SM and is mediated by the massless, electrically neutral gluons. Gluons couple only to color-charged particles such as quarks; the only fermions carrying color charge. Free quarks have never been observed, but can only be found in bound states of quark-antiquark pairs or in bound states of three quarks (or three antiquarks). Multiple quarks in these bound states make up particles called hadrons, where hadrons consisting of three quarks are named baryons and quark-antiquark hadrons are named mesons. Since quarks are spin-1/2 fermions they must obey the exclusion principle, hence the observed Δ^{++} baryon composed of three up-quarks with spin pointing in the same direction should not be able to exist. Therefore an additional quantum number was introduced, the color-charge. A quark can exist in three different color states; red, green or blue, while an antiquark can carry anti-red, anti-green or anti-blue color charge. Thus, even if all up-quarks in Δ^{++} have the same direction of spin they have different color-charges. A color-charged hadron has never been observed, hence the quarks must exist in color neutral combinations such as "red+blue+green" (in analogy to white light being a combination of three primary colors) and e.g. red+anti-red.

In order for the color-charge to be conserved in an interaction, the gluons must simultaneously carry both color- and anticolor-charge. The six different color-states can be linearly combined in 8 different color-anticolor states corresponding to eight physical gluons [8]. Since the gluons can couple to colored particles and they themselves have non-zero color-charges, which implies that gluons can couple to other gluons, they self-interact. The self-interactions lead to properties of the QCD that differ a lot from those of QED, namely asymptotic freedom and color confinement [3].

2.2.1 Screening in QED

The mechanism of screening in QED was introduced to explain the decrease of effective charge at at greater distances. A propagating electron is constantly emitting and absorbing virtual photons that can fluctuate into electron-positron pairs. The Feynman diagram of such a situation is shown in Figure 2.1.

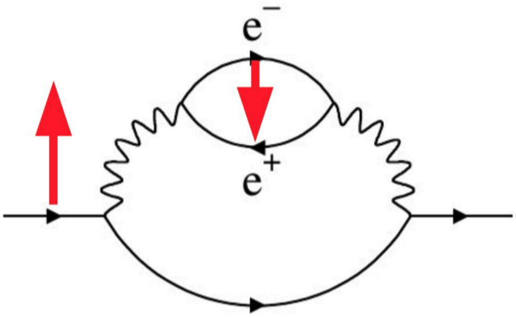

Figure 2.1: Screening in QED where the red arrows represents the electric fields pointing in opposite directions. Figure found in [9]

The virtual electron in each electron-positron loop will attract towards the original electron, while the virtual positron will be repelled away. This will result in vacuum polarization effects where the pairs will screen the charge of the original electron and hence decrease the effective charge in a similar way to what is observed when a charge is embedded in a dielectric medium [10]. When moving away from the original electron, more e^-e^+ pairs will screen the field and this will decrease the electromagnetic force with distance and increase the closer one gets to the original charge.

2.2.2 Screening and Anti-Screening in QCD

Similar to the electron, a quark can emit and absorb gluons that can fluctuate into quark-antiquark pairs that also results in a vacuum polarization effect. This is illustrated in Figure 2.2 where a blue quark (q(b)) emits a red quark (q(r)) and a virtual gluon with blue-antired (b$\overline{r}$) color charge, that in turn split into a q(b) q($\overline{r}$)-pair. The quark-antiquark pair will cause a screening of the color field produced by the original blue charge in exactly the same way the electric charge was screened by the e^-e^+ pairs.

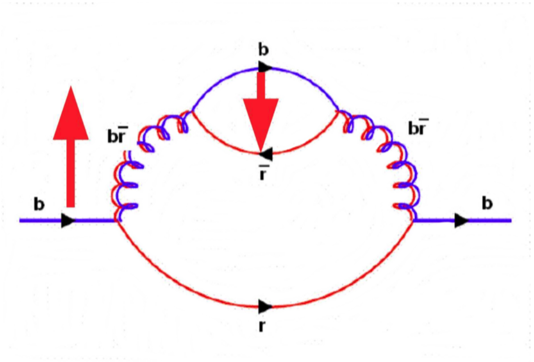

Figure 2.2: Screening in QCD. Figure found in [9]

Because of the self-interaction property of the gluon, it can also happen that the emitted gluon fluctuated into a gluon loop with two gluons. In the case of Figure 2.3, the green charge will create a field that points in the same direction as the color-field of the original blue quark. This results in an anti-screening that enhances the original field. If a particle with color charge is far away from an antiscreening system, it will not see color field originating from the blue quark. Instead it will see a very strong field created by the quark with a large cloud of gluons.

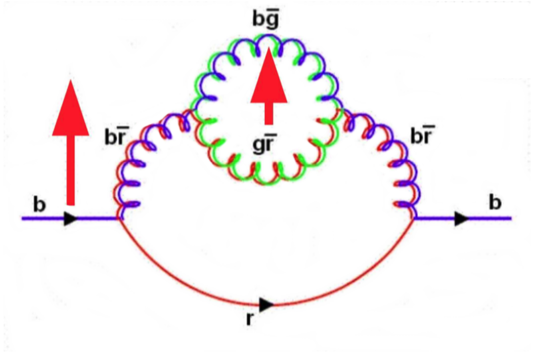

Figure 2.3: Anti-screening in QCD with the color fields pointing in the same direction. Figure found in [9]

The effect of anti-screening in QCD tends to dominate over screening due to the larger color charge of gluons in addition to there being eight gluons and only six quarks.

2.2.3 The Strong Coupling Constant and Asymptotic Freedom

It is not possible to solve the strong force Lagrangian analytically and therefore one has to apply perturbation theory in the high momentum regime in order to solve it [11]. The high momentum regime corresponds to a distance[2] which is much shorter than 1 fm $\sim$

---

[2] The distance at which the strong interaction occurs is related to the momentum transfer, Q, of the interaction. Shorter distance gives larger Q.

200 MeV^{-1}. This approach does however fail in the low momentum regime due to the running of the coupling constant. Due to the screening and anti-screening effects in QCD the strength of the coupling constant, α_s, will vary with the momentum transfer, Q. The variation of α_s as a function of Q is why it is often referred to as the running coupling constant.

At large momentum transfers, $\alpha_s(Q^2)$ is defined as

$$\alpha_s(Q^2) = \frac{\alpha_s(\mu^2)}{1 + \beta_0 \alpha_s(\mu^2) ln\left(\frac{Q^2}{\mu^2}\right)} \tag{1}$$

where $\beta_0 = \frac{1}{12\pi}(11N_c - 2N_f)$; N_c is the number of colors and account for the anti-screening loops, and N_f is the number of quark flavors that account for the screening loops. The three colors and six flavors in the SM give a positive β_0 resulting in a decrease of $\alpha_s(Q^2)$ with increasing Q^2, i.e. the strong coupling gets weaker at large energies. This behavior is known as asymptotic freedom. $\alpha_s(\mu^2)$ in equation (1) is the value of the coupling constant determined at a chosen reference value μ, which is usually taken to be the mass of the Z boson [3].

The magnitude of Λ_{QCD} is used as a scale that separates large values of α_s from small values of α_s in the QCD domain [12]. At energy scales of $Q \gtrsim \Lambda_{QCD}$, the coupling constant becomes sufficiently small, $\alpha_s < 1$, and color charges will approach asymptotic freedom. In this high energy regime perturbative QCD (pQCD) is used to study the strong force and due to the large momentum transfer involved it is referred to the hard QCD domain. If the energy scale instead is at $Q \sim \Lambda_{QCD}$, $\alpha_s \sim 1$, the strong force is too strong for perturbative calculations to be used. These non-perturbative QCD processes are often called the soft QCD domain correspondinig to interactions with low momentum transfer. In the limit of soft QCD color charges are confined due to the very strong force, this effect is called color confinement and will be discussed in the next section.

2.2.4 Color Confinement

The non-observation of free quarks, despite many experimental attempts, can be explained by the color confinement hypothesis [1]. It states that no color-charged particles can propagate freely but have to be confined inside color neutral hadrons. The hypothesis is based on the self-interaction property of the gluon that leads to antiscreening of the color-charge causing α_s to increase with distance between two color-charged particles. It has not been possible to exactly calculate how color confinement works, but it can be qualitatively understood by considering what would happen if one attempts to separate two quarks. The interaction between the quarks will get stronger and stronger, and according to microscopic QCD models, such as the Lund String Model, the gluon field between them form a narrow, one-dimensional, tube (or string) with an almost constant force of $\sim$ 1GeV/fm. The potential energy of the string will increase with distance and eventually it will be energetically favorable for the string to split and form a new $q\bar{q}$-pair, i.e. mesons.

2.2.5 Strongly Interacting Matter in QCD

As previously explained quarks and gluons are confined within hadrons. However, QCD calculations predict that at high enough temperatures and/or particle densities, a phase transition will occur where the hadrons effectively dissolve into deconfined partons. This state of strongly interacting matter is called Quark-Gluon Plasma (QGP).

The quark-gluon plasma can be explained by analogies to the electromagnetic plasma. In the electromagnetic plasma there are mobile charges, described by the Debye screening length λ_D, inside a plasma volume. Moving charges are screened as the electric potential between them decreases exponentially. This can be translated to the asymptotically free color-charged particles in the QGP.

Because of the high temperature created in a heavy-ion collision, there will be a large amount of $q\bar{q}$-pairs produced giving rise to a very dense state. In this state, the λ_D will decrease to a point where it is less than the radius of a given hadron. The hadron will then "melt" into the rest of the plasma volume since the partons of the hadron no longer can identify each other from partons initially belonging to other hadrons. This is due to the decrease of the color-field between the partons, caused by screening. Hence inside this medium in this deconfined state, the quarks and gluons can move as if they are free particles.

2.3 Collision Variables in High-Energy Physics

2.3.1 Center-of-Mass Energy

The center-of-mass energy, $\sqrt{s}$, in a particle collision is the energy that is available for creation of new particles or for exploring the internal structure of particles. s is a Lorentz invariant quantity that can be calculated using the four-momentum vector, $p^\mu = (E, \mathbf{p})$, of each particle. E is the energy of the particle while $\mathbf{p}$ is its three-momentum. For two particles travelling towards each other with four-momentum p_1 and p_2 and with equal energy, three-momentum, and mass the center-of-mass energy can be calculated by inserting this information into the definition of s, $s = (p_1 + p_2)^2$, which gives

$$s = (p_1 + p_2)^2 = (E^2 - |\mathbf{p}|^2) + (E^2 - |\mathbf{p}|^2) + 2(E^2 + |\mathbf{p}|^2) = 4E^2 \implies \sqrt{s} = 2E$$

For this thesis, pp collisions with a $\sqrt{s} = 13$ TeV have been analyzed, which implies that the proton beams had an energy of 6.5 TeV each.

2.3.2 Transverse momentum

The transverse momentum, p_T, of a particle is the fraction of momentum in the plane perpendicular to the beam line direction (usually defined as the z-axis). The perpendicular plane is defined with the horizontal x-axis and vertical y-axis. Hence, p_T is defined as,

$$p_T = \sqrt{p_x^2 + p_y^2}. \tag{2}$$

p_T is of interest since it is initially 0 for incoming particles before they collide, thus when observed it can give information about the dynamics of the collision, e.g. higher p_T particles are associated with hard collisions while lower p_T particles are associated with soft collisions [6].

2.3.3 Rapidity and Pseudorapidity

The investigated particles will have relativistic energies and it is therefore useful to use rapidity, y, to measure the longitudinal momentum of the particles. Since rapidity is additive under Lorentz boosts along the beam-line it is used instead of the standard velocity. y is defined as

$$y = \frac{1}{2} \ln \left(\frac{E + p_z}{E - p_z} \right) \tag{3}$$

where $E = \sqrt{m^2 + p^2}$ is the total energy of the particle, m the mass of the particle, p its total momentum and p_z is the momentum of the particle in z-direction [6]. Considering that the masses of the produced particles are hard to measure, it complicates the calculations of the mass-dependent rapidity.

Therefore one often uses an approximation of y which is the mass-independent pseudorapidity η:

$$\eta = \frac{1}{2} \ln \left(\frac{|\vec{p}| + p_z}{|\vec{p}| - p_z} \right) = -\ln \left(\tan \frac{\theta}{2} \right) \tag{4}$$

where θ is the polar angle. The pseudorapidity is almost equal to rapidity for p_T much greater than the mass and can thus inherit the Lorentz additive invariance from the rapidity. An expression that will be used later in this thesis is mid-rapidity. The mid-rapidity region (also called central rapidity region) is the region in the center-of-mass frame where $|y| \approx |\eta| < 1$ [6]. Particles in this region are of interest since this is the region with the largest density dN/dy, and the farthest from the initial beam particles. Rapidity (pseudorapidty) values of $y(\eta) > 0$ or $y(\eta) < 0$ tells us if the particle moved in the forward or backward direction respectively.

2.3.4 Collision Centrality and multiplicity

In ultra-relativistic heavy-ion experiments the collision centrality is estimated using the impact parameter b, which is defined as the distance between the centers of the two nuclei in the plane transverse to the direction of motion. Since it is not possible to directly measure the impact parameter in a collision, one has to use other experimental observables that has a direct correspondence to the collision centrality. One such observable is the charged-particle multiplicity that measures the number of particles detected in the collision. Before the nuclei collide they will be Lorentz contracted in the direction of motion due to ultra-relativistic effects, hence they will appear as two thin discs. If the length of the impact parameter is small enough such that there is an overlap region of the two nuclei, there is a possibility for the nucleons to interact. The nucleons that participate in the interaction are called participants, while the non-interacting nucleons are referred to as spectators. A central collision corresponds to a very small impact parameter, $b \to 0$, with a large overlapping region of participants will produce a large number of particles, i.e. high multiplicity. If, however, b is large, the volume of participants is small resulting in low multiplicity, this is referred to a peripheral collision.

There is, as mentioned, a direct correlation between centrality and multiplicity in heavy-ion collisions. This correlation is much less clear when colliding two protons [11]. The participants in pp collisions will instead of the nucleons in heavy-ion collisions, be the inelastically scattered partons, i.e. quarks and gluons, in the proton. These multiple parton-parton collisions will from hereon be called MultiParton Interactions (MPIs). The interacting partons will produce new particles and multiplicity can still be used to estimate the number of participants. More partons will interact in a central collision resulting in high multiplicities, and less in a peripheral collision resulting in low multiplicities. The difference between heavy-ion and pp collisions is that the initial state geometry is known for heavy-ions while it is not given for the protons, thus the final state particles, i.e. the multiplicities, is one of the main properties describing pp collisions.

2.3.5 Transverse Spherocity

The mid-rapidity charged hadron transverse spherocity, S_0, is used as a selection to extract more information from data by looking at event shapes. More specifically it is used to categorize the events through the geometrical distribution of p_T of the charged hadrons. It is restricted to the transverse plane in order to avoid the bias from the boost along the beam axis. The S_0 is defined as

$$S_0 = \frac{\pi^2}{4}\left(\frac{\sum_i |\vec{p_{T_i}} \times \hat{n}|}{\sum_i p_{T_i}}\right)^2$$

where $\vec{n}$ is the transverse unit vector chosen in a way such that it minimizes the ratio. The unit vector coincides with one of the p_T-vectors which by construction gives two limits to S_0:

$$S_0 = \begin{cases} 0 & \text{"jetty" limit (hard QCD events)} \\ 1 & \text{"isotropic" limit (soft QCD events)} \end{cases}$$

The value of S_0 gives an indication of the geometrical distribution in the event plane. An uneven collision distribution of charged hadrons will give a "pencil-like" geometrical shape of the event with a S_0-value going towards 0. These events will be characterized as jetty events where hard QCD processes dominate. The more evenly distributed collision events will have a S_0-value going towards 1, these will be characterized as isotropic where soft QCD processes dominate.

3 Quark-Gluon Plasma

In the first few microseconds after the Big Bang, when our Universe was extremely hot with zero net baryon number density, it is believed that it was in a quark-gluon plasma state [6]. The temperature dropped with the expansion of the Universe and it entered the hadronic gas phase [9]. Today the QGP might exist in the core of very heavy neutron stars with an environment that is different from the early Universe. The core of a neutron star has a relatively low temperature but instead it has high enough baryon number density in order to create the plasma.

The extreme conditions needed for hadronic matter to phase transition into QGP can today be achieved in high-energy heavy-ion collider experiments, such as the ALICE experiment at LHC described in section 4. These conditions are the critical temperature, T_c, of $\sim$ 160 MeV and an energy density, ϵ, of $\sim$ 1 Gev/fm^3 [13]. The plasma created in a nuclear collision contains much less energy in comparison to the one created after the Big Bang, which results in a much shorter life time of about 10^{-22}s compared to 10^{-5}s [14]. Partons in the QGP will start to hadronize (transform back into hadronic matter) after 10^{-22}s and it is therefore impossible to directly study the plasma. Instead one has to use the final state particles in order to study the observable characteristics of the QGP.

3.1 Quark-Gluon Plasma in Large Systems

In relativistic heavy-ion collisions, also known as large systems, it is possible to reach high enough energy densities in order to study the different stages of QGP; the QGP formation, expansion, hadronization, and the freeze-out stage. In the formation of the QGP, before the system is in equilibrium, the initial partonic collisions will produce a fireball that is in a highly excited state. The frequent collisions of the fireball constituents will establish a local equilibrium state and the time it takes to reach this equilibrium is often referred to as the thermalization time. In this thermalized state the partons in the QGP will be deconfined [11].

After the production of QGP, the system will have a thermal pressure acting on the surrounding vacuum. Becuase of this pressure, the QGP will undergo a collective expansion leading to a decrease in energy density and the system cools down. As the temperature decreases and eventually is below T_c, the deconfined partons will start to hadronize. In the hadronization stage the plasma expands again, this time very rapidly and over a small temperature interval. This part is not a fully understood process [11].

The last stage before the hadrons propagate to the detectors is the freeze-out stage that goes in two steps; the chemical and the kinetic freeze-out. In the chemical freeze-out stage, after the hadronization, the system is in thermal equilibrium and the local equilibrium is maintained by the frequently colliding hadrons. The medium continues to expand and decrease in temperature. The number of inelastic collisions (allowing hadrons to change identity) becomes too small compared to the rate of the expansion, hence the hadron abundances are fixed. As the system continues to further expand, there will come a stage where the average distance between hadrons becomes larger than the range of the strong interaction. The hadron collisions inside the QGP will not be frequent enough to maintain local equilibrium and the collective description does not hold anymore, this is what is referred to as the kinetic freeze-out [11].

3.2 Observables of the QGP

The QGP is expected to be produced when colliding ultra-relativistic heavy ions (such as lead or gold). It is however, not possible to study the transient QGP state directly, and therefore, any information about it has to be obtained from the detected final-state particles. In order to get information from these particles, one has to know which observables that indicate a formation of QGP [11]. The observables relevant for the analysis in this thesis are presented below.

3.2.1 Collective Flow

The collective expansion in the early stage of the QGP evolution, before hadronization, will generate radial and anisotropic flow of the medium. If a heavy-ion collision is central, the density of the created plasma will decrease from the center of the medium to its edges [12], giving rise to a pressure gradient acting on the surrounding vacuum. The radially symmetric pressure gradient will then boost the hadrons with a radial velocity $\mathbf{v}$, giving rise to radial flow and according to $\mathbf{p} = \gamma m \mathbf{v}$, heavier hadrons will gain larger momenta than the lighter hadrons. The radial flow will then cause the abundance of low-p_T hadrons to shift towards higher p_T. This mass hierarchy of the p_T distributions are shown in Figure 3.1.

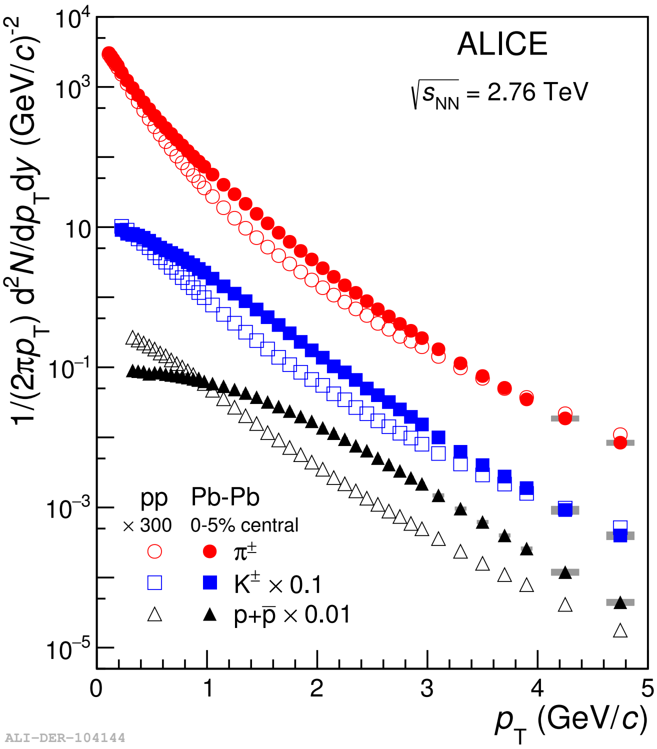

Figure 3.1: The p_T distribution of pions, kaons and protons in pp and Pb-Pb collisions. The hadrons fron the Pb-Pb collisions indicates a boost to higher p_T compared to the hadrons from pp collisions. This effect is larger for heavier hadrons. Figure found in [15].

Figure 3.2 shows an enhanced baryon-to-meson ratio at intermediate p_T in central heavy-ion collisions when compared to peripheral heavy-ion or pp collisions that has been observed at both RHIC and ALICE [15]. The clearly enhanced peak around 3 GeV/c and a little above, for kaons and protons respectively, can be interpreted with a hydrodynamic description [15] where the enhanced ratio can be described with the mass dependence of radial flow.

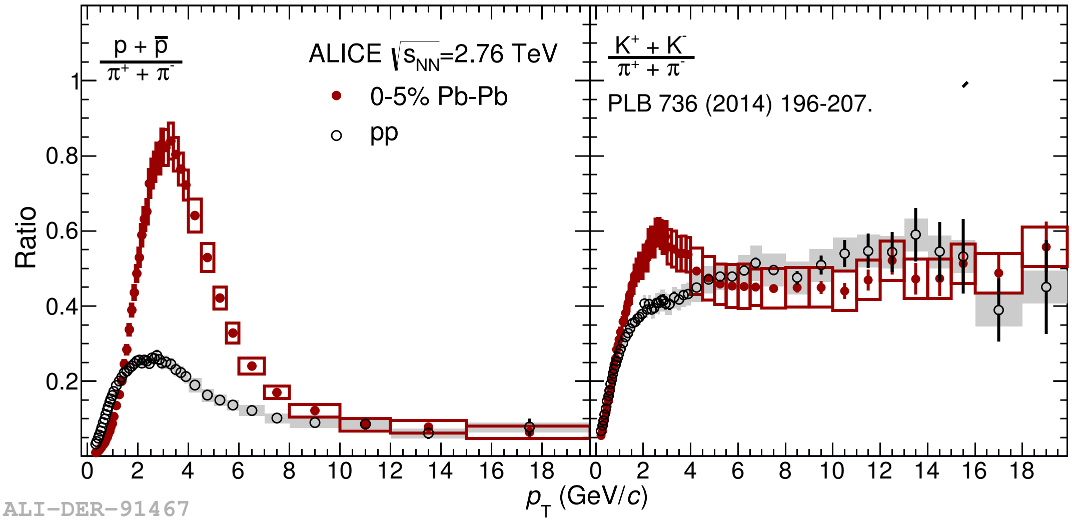

Figure 3.2: The baryon-to-meson ratio for protons and kaons over pions for pp and Pb-Pb collisions as a function of p_T. Figure found in [15].

In practice, hadrons and nuclei are never completely central, i.e. the pressure gradients are never completely radially symmetric. Therefore the collision geometry is an important factor for anisotropic flow. Figure 3.3 shows a semi-central heavy-ion collision giving rise to the second order flow, or elliptic flow, which is the dominant contribution for anisotropic flow in less central heavy-ion collisions. The overlap region of the colliding nuclei will give an almond shaped collision volume leading to the pressure gradient being larger in the x direction than in the y direction. This means that hadrons that are pushed outwards, receives a larger flow velocity in the reaction plane (x, z) than perpendicular to it, giving an anisotropic momentum distribution of the particles.

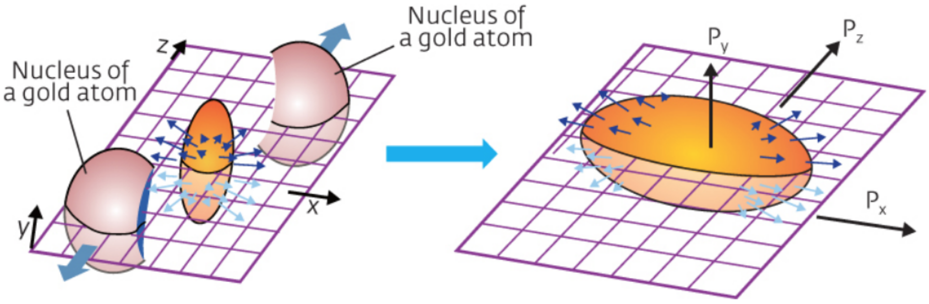

Figure 3.3: The geometry of a semi-central Au-Au collision. Figure taken from [12]

The momentum anisotropy can be expressed with a Fourier expansion where the flow harmonics, v_n, are the Fourier coefficients. Each harmonic, v_n, corresponds to different anisotropic flow. Elliptic flow is given by the second Fourier coefficient v_2, where the almond shaped collision-volume produces the highest v_2 values. A measurement of elliptic flow can be done using two particle correlations which will be explained in section 5.2. The result of such a measurement will give rise to what is often referred to a double ridge, see Figure 3.4. Some characteristic features of the double ridge is the near side jet peak structure at $(\Delta\phi, \Delta\eta)$=(0,0) and the away side peak at $\Delta\phi = \pi$ and is elongated in $\Delta\eta$. The near-side peak represents two particles of the same jet, and the away-side peak represents two particles in back-to-back jets. In heavy-ion collisions, there is an additional feature of a structure at $\Delta\phi = 0$ also elongated in $\Delta\eta$. These two elongated structures is what constructs the double ridge [16].

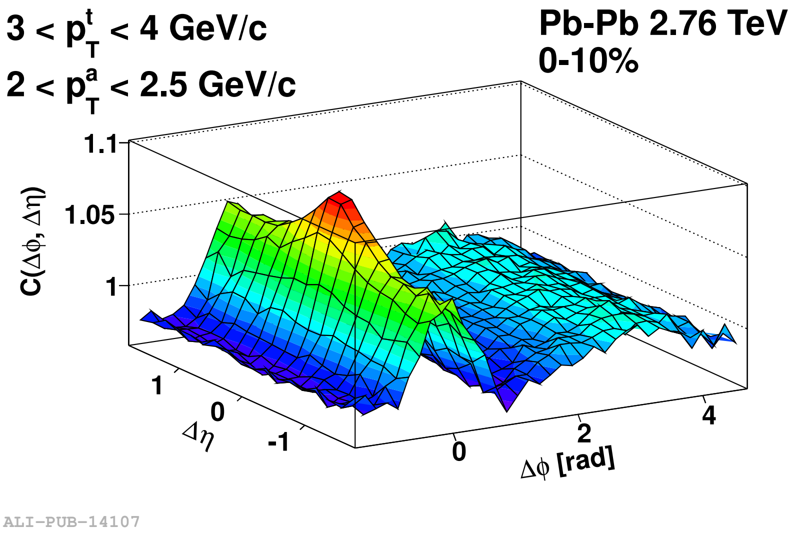

Figure 3.4: Measurement of elliptic flow using two particle correlations for high-multiplicity Pb-Pb collisions. Figure taken from [17]

3.2.2 Strangeness Enhancement

Strangeness enhancement; an enhanced production of strange hadrons (hadrons composed of one or several s quarks), was originally proposed [18] as a QGP observable in heavy-ion collisions where the conditions needed to form QGP were achieved. This enhancement was experimentally observed when comparing the production of strange hadrons in heavy-ion collisions compared to pp and p-A collisions [19], with a larger enhancement the more s quarks that are contained in the strange hadron.

Since the s quarks are not initially present in the colliding hadrons, like the u and d quarks, they must have been produced in the collision. Due to the hard scattering partons in a collision, the strange quarks can be produced in $q\bar{q} \rightarrow s\bar{s}$ and $g\bar{g} \rightarrow s\bar{s}$ reactions where the fusion of gluons dominates the production [11]. The deconfined quarks and gluons in the QGP lowers the minimum momentum transfer needed for the reactions to occur since it is the bare mass of the s quark that determines the momentum transfer instead of its constituent mass as it would have been in a hadronic gas [20]. Hence, it is expected that the production of strange quarks is larger in a collision where a QGP was formed than in a collision where it was not formed.

3.3 QGP in Small Systems

In order to draw conclusions of the QGP properties in heavy-ion collisions, one has to compare it to reference data of understood processes where it is believed that no plasma was formed. Historically small systems, such as pp and p-A collisions, have been used as reference data. However, it has recently been discovered that these systems exhibit similar collective behaviour to those in large systems. For example, flow like behaviour, represented as the double ridge, was observed for high-multiplicity pp and p-Pb collisions at the ALICE, ATLAS and CMS experiments at LHC [21] [22] [23]. There has also been an observation of strangeness enhancement at high-multiplicity pp collisions made by the ALICE experiment and is shown in Figure 3.5. These observations may indicate that QGP is formed in small systems as well, but could also be due to initial state effects.

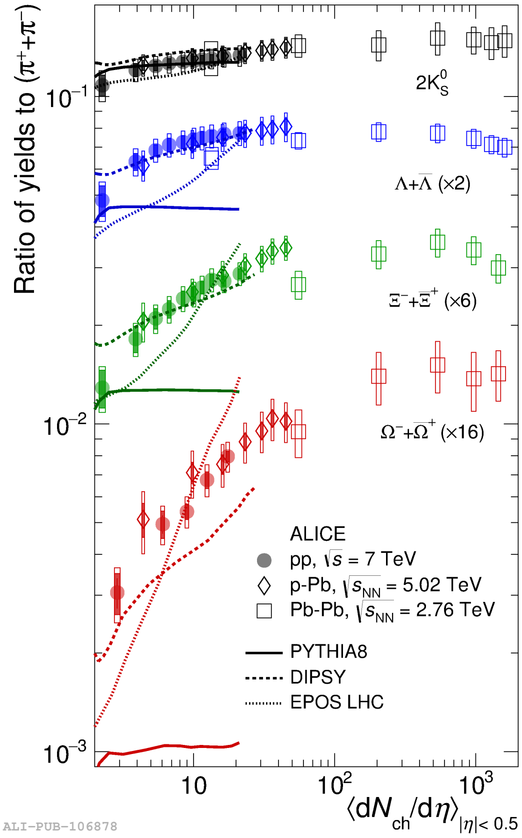

Figure 3.5: Results of strangeness enhancement in high-multiplicity pp collisions where the p_T-integrated strange hadron yield is shown as a function of multiplicity. More information and figure found in paper[24].

3.4 Microscopic Models

3.4.1 Lund String Model

The Lund String Model, which is implemented in microscopic Monte Carlo generators such as PYTHIA [25], is a microscopic QCD model attempting to describe how partons can create new hadrons in a particle collision, a process called hadronization. In a particle collision, the colliding quarks will form gluon color fields between them and in the Lund string model these color fields are seen as strings with tension $\kappa = 1$ GeV/fm. For simplicity, consider a quark and an anti-quark, the further apart they move from each other the more potential energy is contained in the string. The potential energy will increase with distance until it is energetically favorable to create a pair of mesons and break the string.

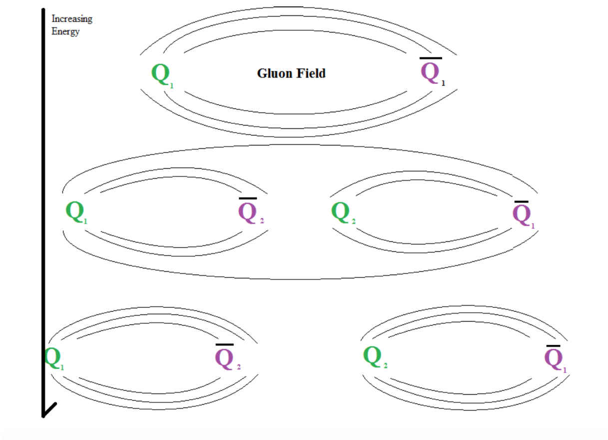

Figure 3.6: An illustrative figure of the Lund String model, where a $q\bar{q}$ pair is produced as the color field, string, expands.[26]

Hadronization occurs in all collisions and is a term often used to describe soft QCD processes. In these processes, a gluon color field will span between the quarks and the hadronization will occur isotropically. If instead a hard QCD process occurs, a lot of energy is transferred to a quark or a gluon, i.e. a lot of potential energy will be stored in the color fields, so much that it will cause hadronization chain-reactions. The process described in Figure 3.6 will then repeat for the newly created $q\bar{q}$ pairs until the original energy is dissipated. This will in turn give rise to hadron showers that is focused in cones directed away from the beam-axis. These hadron showers are referred to as jets, and since they are easy to identify in particle detectors they are used as an indication that hard processes occurred in a collision.

3.4.2 Rope Hadronization

A microscopic model for collectivity has been implemented in PYTHIA8, referred to as the Rope Hadronization framework. This model is based on interacting Lund-strings such as *rope hadronization* and *string shoving*. The rope hadronization model provides a correction to the previous mentioned Lund string hadronization model where the semi-classical string has a tension of 1 GeV/fm. The correction is made by allowing the strings to overlap in the transverse space and hence act coherently as a "rope" [27]. These strings will then hadronize, possibly as color multiplets with a higher effective string tension called flavor ropes; leading to an increased likelyhood of producing heavier quarks such as the strange quark. String shoving is an extension to the rope hadronization model where the overlap of the strings generates a transverse pressure, giving rise to a transverse flow. Rope hadronization and string shoving provides a good description of strangeness enhancement (in both big and small collision systems) and the ridge in pp collisions, respectively. A more detailed explanation is given in [27, 28, 29].

4 The ALICE Experiment at LHC

At the European Organisation of Nuclear Research (CERN), located in Geneva Switzerland, you will find the largest and most powerful particle accelerator in the world, namely the Large Hadron Collider (LHC). The LHC is a circular particle synchrotron of 27 km in circumference with 1000 superconducting magnets that bend and focus the beam-line [30]. It is designed to study fundamental particles and how they interact by colliding beams of protons or heavy ions with a maximum center-of-mass energy $\sqrt{s} = 14$ TeV for pp collisions and $\sqrt{s_{NN}} = 5.5$ for Pb-Pb collisions [31]. As of today, center-of-mass energies of 13 TeV and 5.02 TeV are achieved for pp and Pb-Pb, respectively. The LHC has four intersection points where the beams collide and each point has its own experiment; ATLAS [32], CMS [33], LHCb [34] and ALICE.

ALICE, an acronym for a Large Ion Collider Experiment, is the detector used to record the data used for the analysis in this thesis and the only experiment at LHC dedicated to heavy-ion physics with a focus on strongly interacting matter and the QGP [35]. It is optimized for a low transverse momentum threshold of $p_T^{min} \sim 0.15$ GeV/c and particle identification capabilities up to 20 GeV/c [36]. The dimensions of the ALICE detector are 16x16x26 m^3 and weighs about 10000 t. ALICE is situated 56 m underground and consists of 17 different detection systems which are shown in Figure 4.1.

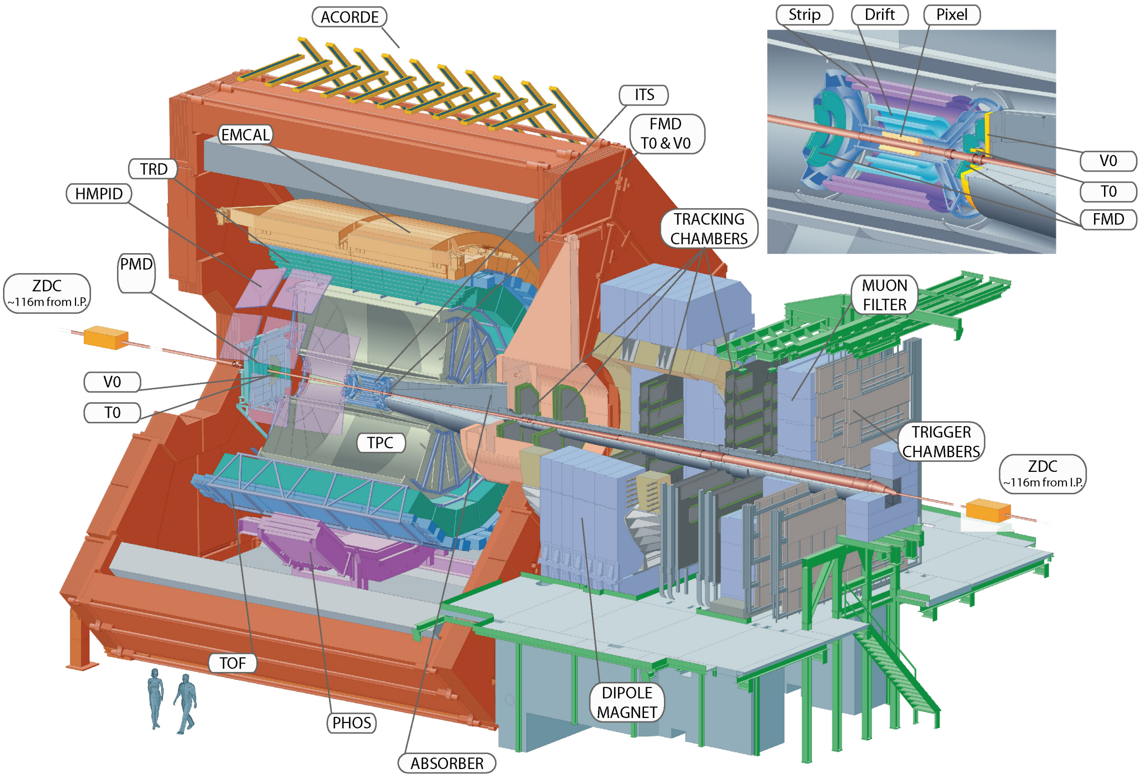

Figure 4.1: A schematic figure of the sub-detectors in ALICE. Figure taken from [36]

4.1 ALICE Detector Systems

The 17 different detector systems are divided up into three different categories; central barrel detectors, forward detectors and the MUON spectrometer. The central barrel detectors are the Inner Tracking System (ITS), Time Projection Chamber (TPC), Transition Radiation Detector (TRD), Photon Spectrometer (PHOS), Electromagnetic Calorimeter (EMCal) and the High Momentum Particle Identification Detector (HMPID). All of these detectors are enclosed in a solenoid magnet that generates a magnetic field of up to $B = 0.5$ T [36]. The main tracking detectors in ALICE are the ITS and the TPC, in which the trajectories of charged particles in space are reconstructed and the particles momentum measured.For information about the particles identity, additional detectors are needed. The TOF measures the time it takes for the particles to travel from the interaction point to the detector, with a high precision. With this information the speed of the particles can be measured. The HMPID identifies high-p_T particles, while the TRD identifies the electrons. EMCal and PHOS measures the energy of the electrons and photons, respectively, by absorbing the energy of the particles as they traverse and interact with the dense materials of the detectors.

The forward detectors of ALICE include the Photon Multiplicity Detector (PMD), the silicon Forward Multiplicity Detector (FMD), Zero Degree Calorimeter (ZDC), the quartz Cherenkov detector T0, and the plastic scintillator detector VZERO. They are referred to as the *forward* detectors due to their position close to the beam-line. The PMD and FMD measures photons and charged particles at $|\eta| \sim 3$. The T0 detector measures the time and the longitudinal position of the interaction. The VZERO and ZDC detectors, both determines the centrality of the collision [36]. The multiplicity selections in this thesis was made using the VZERO detector. The muon spectrometer measures the quarkonia and light vector meson production down to very low p_T with a large rapidity range $-4.0 < y < -2.5$ [36].

4.1.1 Time Projection Chamber

The main tracking detector in ALICE is the Time Projection Chamber (TPC), seen in Figure 4.2, with a coverage of the full azimuth and the mid-rapidity region of $|\eta| < 0.9$. It is used to provide tracking of particles, measurements of charged particle momentum, particle identification and two-track separation. It is located in the central barrel of ALICE (surrounding the ITS) aligned with the beam-line and parallel to the magnetic field of the central barrel. The TPC is a hollow cylinder with a drift volume of 88 m^3 filled with a Ne-CO_2 gas mixture.

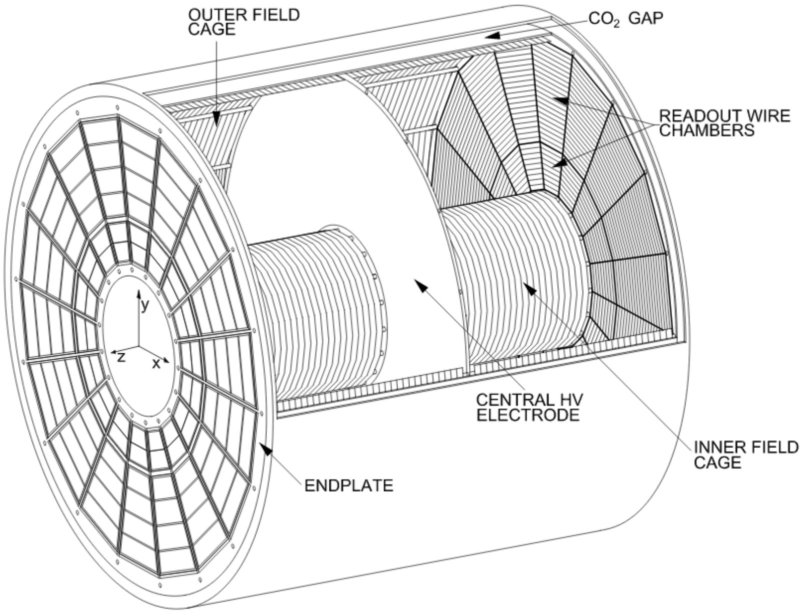

Figure 4.2: A schematic sketch of the TPC in ALICE. Figure taken from [37].

The Multi-Wire Proportional Chambers (MWPCs) located at the end-plates will detect the electrons and amplify the signal through an avalanche of ionized particles and electrons. By measuring the drift time of the particle, it is possible to reconstruct a three-dimensional image of the ionized particle track. This is done by reading out the MWPC signal and translate it into the x and y coordinates, while the drift time and known drift velocity is used in order to get the z component. The trajectory of the ionized particle will have a curvature due to the magnetic field and this curvature is used to determine the momentum of the particle.

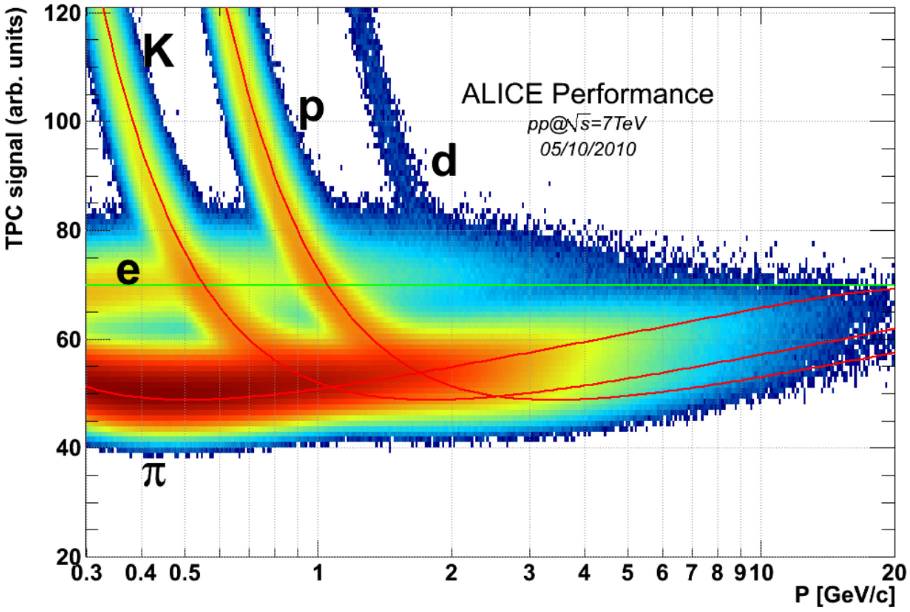

Figure 4.3: The energy loss per distance unit (dE/dx) as a function of momentum for electrons, pions, Kaons, protons and deutrons. Figure taken from [38]

Particle identification with the TPC is the done by measuring the specific energy lodd (dE/dx), charge and momentum for each particle going through the detector gas [36]. The energy loss is described by the Bethe-Bloch formula that includes particle specific properties and is therefore used when identifying particles [9]. The formula is defined as

$$\left\langle \frac{dE}{dx} \right\rangle = \frac{4N\pi N e^4}{m_e c^2} \cdot \frac{z^2}{\beta^2} \cdot \left(\ln \frac{2mc^2\beta^2\gamma^2}{I^2} - \beta^2 - \frac{\delta(\beta)}{2} \right)$$

where N is the electron density of the material, e the elementary charge, $m_e c^2$ the rest energy of the electron, z the charge of the particle traversing the detector, m the particle mass, and I the mean gas atom excitation potential. $\beta = v/c$ is the relative velocity, $\gamma = 1/\sqrt{1-\beta^2}$ is the Lorentz factor, and $\beta\gamma = p/mc$) which lets the energy loss be a function of momentum instead of β [9]. Hence, different kinds of particles will generate different bands depending on the mass and charge of the particle. These bands can be seen in Figure 4.3.

4.1.2 The VZERO Detector

The VZERO system is used for centrality measurements as well as measurements of beam luminosity, charged particle multiplicity and azimuthal distributions [39]. The detector consists of two scintillator detectors, VZERO-A and VZERO-C shown in Figure 4.4 together with the ITS, that are placed in the forward direction and covers pseudorapidity ranges of $2.8 < \eta < 5.1$ and $-3.7 < \eta < -1.7$, respectively. As a charged particle traverse the scintillator detector, it will excite and ionize the atoms in the scintillating material. The excess energy of these atoms will be emitted as photons, where the number of emitted photons is proportional to the energy deposited by the incoming charged particle. The emitted photons will then enter Photo Multiplier Tubes (PMTs) where they will hit photo cathodes and emit electrons that are accelerated towards a positive voltage. The accelerated electrons will cause electron avalanches giving rise to an amplified signal before it is read out by the VZERO front-end electronics.

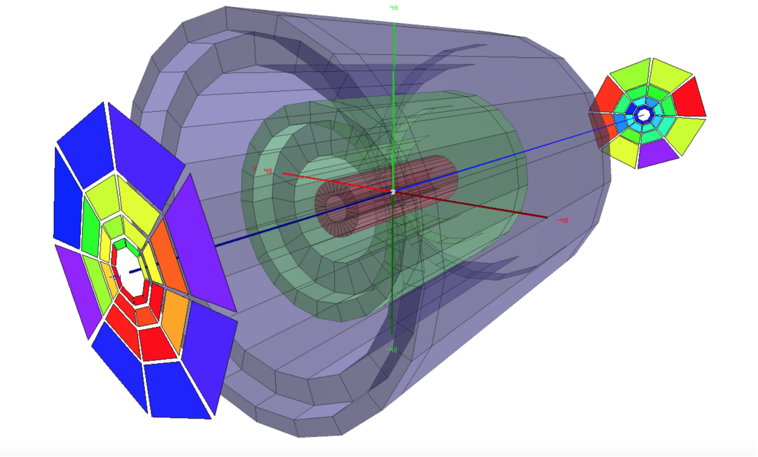

Figure 4.4: A display of the two VZERO detectors with ITS detector in between. Figure taken from [40]

The VZERO detector measures the multiplicity of a collision based on the deposited energy in the scintillators, where the signal amplitude from both VZERO-A and VZERO-C will be referred to as the V0M amplitude. An example of a typical distribution of V0M amplitudes for a number of events is shown in Figure 4.5 and these distributions are used for multiplicity selections. A high V0M amplitude corresponds to a central collision with many produced particles, while a low V0M amplitude corresponds to a peripheral collision with less produced particles. The V0M class of 0-5% represents the 5% of the total number of collisions with the highest V0M amplitude, i.e. the 5% of the events with highest multiplicity.

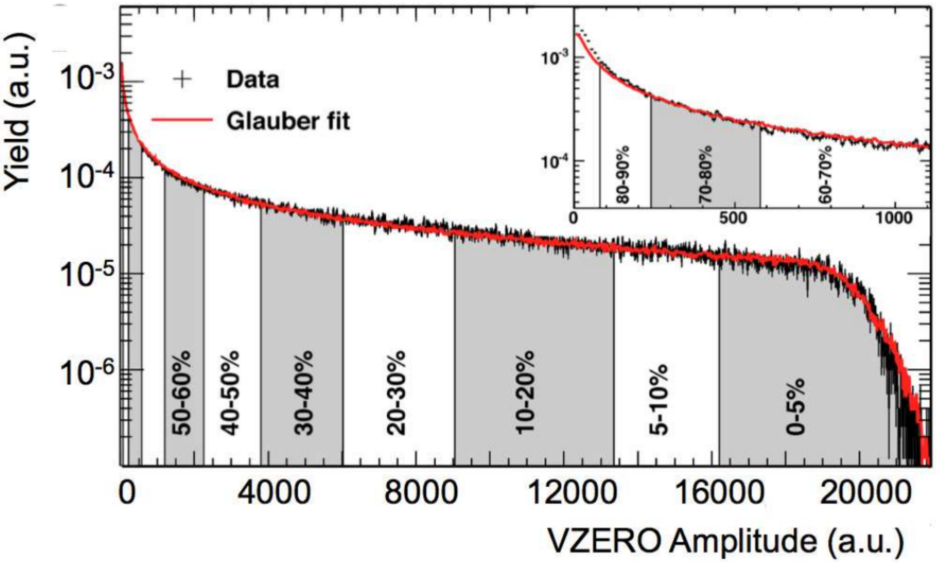

Figure 4.5: An example of the distribution of the v0M amplitudes (the sum of amplitudes from VZERO-A and VZERO-C) where the centrality classes are shown; low percentage means high multiplicity while high percentage means low multiplicity. Figure taken from [39]

5 Analysis

For this thesis two parallel analyses have been performed; one simulation study using PYTHIA and one data analysis. In the simulation study, different and newly developed estimators were tested on different QGP observables and monte-carlo data sets. From the results of the simulation study an estimator and an observable were selected and tested on a real data set.

5.1 Data Processing

The software used to generate the results for this analysis was AliROOT which is the Off-line framework for simulation, reconstruction and analysis used within the ALICE collaboration [41]. The framework and all applications of AliROOT is built upon a foundation of the ROOT [42] system. ROOT is a high-energy physics software designed for processing petabytes of data in an efficient way. It was developed at CERN and is an object-oriented C++ framework [42].

5.2 Two-Particle Correlations

Two-particle correlations were used to construct and study the double ridge. It is a powerful tool to study particle production and collective effects of hadron and heavy ion collisions at high beam energy. The particle correlations are measured over distributions in relative azimuthal angle, $\Delta\phi = \phi_{trig} - \phi_{assoc}$, and relative pseudorapidity angle, $\Delta\eta = \eta_{trig} - \eta_{assoc}$. The two particles are chosen from different p_T regions, a trigger particle within a p_T interval of $2 < p_{T,trig} < 4$ GeV/c and an associated particle within $1 < p_{T,assoc} < 2$ GeV/c. These p_T ranges was used since this is where the ridge effect is large and the statistics is still good. The associated yield per trigger particle is then measured as a function of the azimuthal angle difference $\Delta\phi$ and difference in pseudorapidity $\Delta\eta$:

$$\frac{1}{N_{trig}}\frac{d^2N_{assoc}}{d\Delta\eta d\Delta\phi} = \frac{S(\Delta\eta,\Delta\phi)}{B(\Delta\eta,\Delta\phi)} \tag{5}$$

where N_{trig} is the number of trigger particles in the event that is within the $p_{T,trig}$ interval [21].

The signal distribution, $S(\Delta\eta,\Delta\phi)$, is given by $\frac{1}{N_{trig}}\frac{d^2N_{same}}{d\Delta\eta d\Delta\phi}$, which is the associated yield per trigger particle for pairs of particles from the same event. Due to the η acceptance of the detector, the particle pairs from the same event gives a triangular distribution in $\Delta\eta$, seen in Fig.5.1.

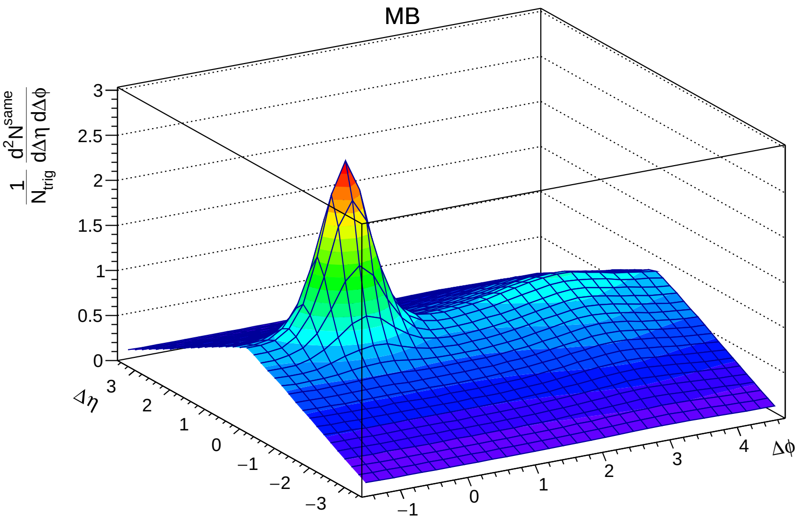

Figure 5.1: The signal distribution with pairs from the same event.

5.2.1 Background reduction and Event mixing

In order to get the corrected associated yield per trigger particle, two steps are performed on the same pair correlations. The event mixing technique was used to get the background distribution, $B(\Delta\eta,\Delta\phi) = \alpha\frac{d^2N_{mixed}}{d\Delta\eta d\Delta\phi}$. For the event mixing, the associated yield per trigger particle is again constructed, but now the trigger and the associated particle were correlated from different events. In this analysis each event was mixed with 10 events. The background distribution (Fig.5.2) was normalized with the α factor which is chosen such that $B(\Delta\eta \approx 0, \Delta\phi \approx 0) = 1$ [21]. The idea is that the mixed event distribution should correct for holes and edges of the acceptance and these cannot be at (0,0).

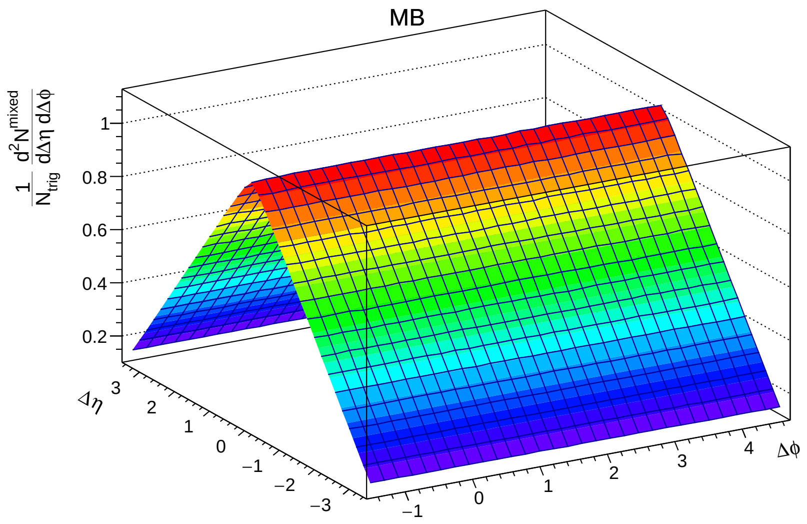

Figure 5.2: The background distribution with mixed event pairs.

The next step was to take the ratio of the pair distributions from the same and mixed events as in Eq.5 in order to obtain the corrected distribution shown in Fig.5.3.

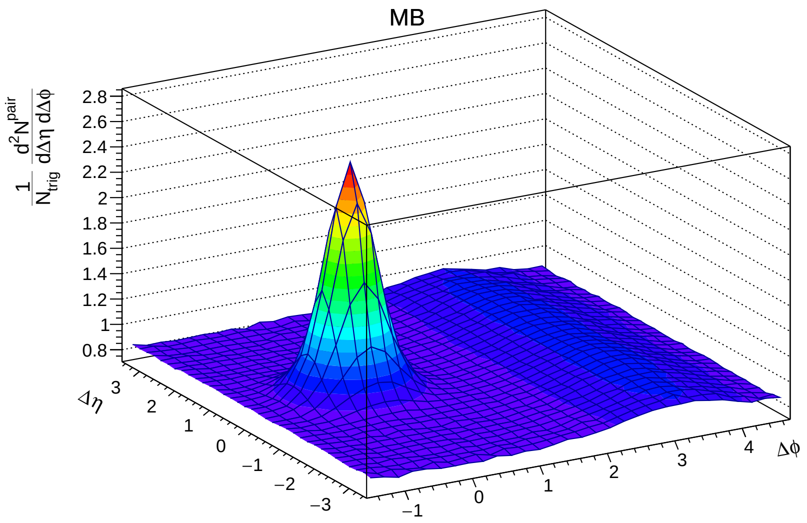

Figure 5.3: The background corrected signal distribution.

5.3 PYTHIA Studies

5.3.1 Monte Carlo Data Sets and Rope Hadronization

Monte Carlo simulations were used in order to investigate different kinds of estimators. These simulations are given by event generators that in agreement with theories and models produce artificial systems of particles in collisions. PYTHIA [25] version 8240 was used to generate three different data sets with 5×10^6 pp collision events at $\sqrt{s} = 13$ TeV each. The properties of all particles in the generated collisions are known, and each type of particle is assigned a unique Particle Data Group (PDG) code that holds all that information. The PDG codes were used when analyzing radial flow and strangeness enhancement.

The microscopic model for collectivity was used when generating two out of three data sets for this analysis. The different data sets will be denoted Default, Strange, and Flow depending on their properties. The Default data set uses the regular PYTHIA MPI model (Lund string model) with no extra models added when generating the data set. In order to enable the microscopic model in the Strange and Flow data set one has to "switch on" the Rope Hadronization framework. Within this framework there are two different flags, one called doFlavour which is used in the Strange data set to enable the flow rope model and another called doShoving used to generate the Flow data set which enables the string shoving model. An overview can be seen in Table 3 and the actual code used in order to produce the different data sets is found in Appendix A. Information about the Rope Hadronization framework can be found in [43].

Table 3: An overview of the models used in the different data sets.

	Rope Hadr. frame.	**doShoving**	**doFlavour**
Default	off	off	off
Strange	on	off	on
Flow	on	on	off

5.3.2 Estimators

Three different QGP-estimators were investigated in this analysis; Transverse Spherocity, an altered version of Transverse Spherocity, and a new technique which combine measurements from mid and forward rapidity ranges that has been decided to call the Mid-Forward estimator. A general problem in small systems is that possible medium effects are small and can be obscured by hard collisions. Therefore the idea of these estimators was to use them as a tool to separate high multiplicity isotropic events, where the medium effects are enhanced, from high multiplicity jetty events.

All three estimators was tested using the three different data sets and by looking at three different observables; the double ridge, radial flow and strangeness enhancement. As such, there are several permutations of each physics signature. The V0M high multiplicity analysis was done on the accepted events for all three estimators. The total distribution of these events as a function of V0M amplitudes is shown in Figure 5.4, where the 10% with highest V0M amplitudes are selected to be high multiplicity events shown in green.

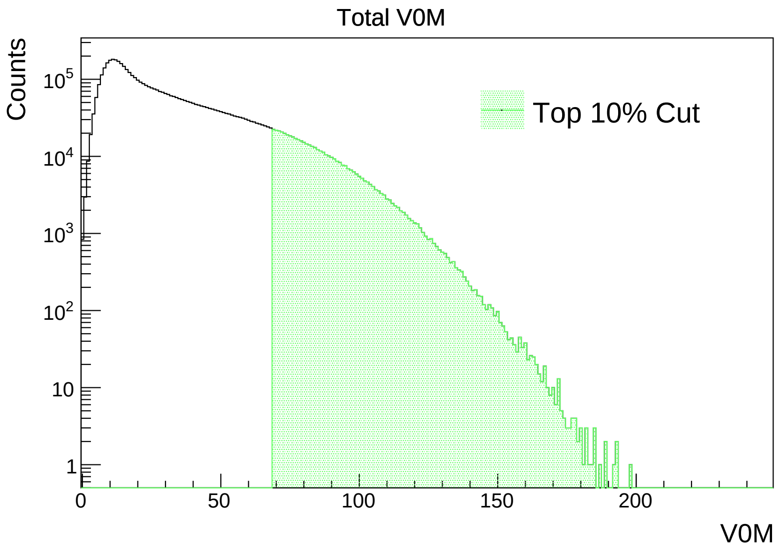

Figure 5.4: The V0M multiplicity distribution for pp collisions at $\sqrt{s} = 13$ TeV with the high Multiplicity selection cut in green.

5.3.2.1 Transverse Spherocity The Transverse Spherocity estimator requires the high multiplicity events to have at least 10 tracks within the mid-pseudorapidity range of $|\eta| < 0.8$. The total distribution of all accepted events as a function of spherocity, S_0, is shown in Figure 5.5. From this distribution two cuts were applied; 20% of the accepted events with the lowest and highest spherocity values were selected as jetty and isotropic events, respectively. The two different cuts are visualized in Figure 5.5, the jetty events in blue and the isotropic events in red. Depending on which data set that was used, the spherocity cut values differed because of a shift of the peak towards higher S_0. The different values are shown in Table 4.

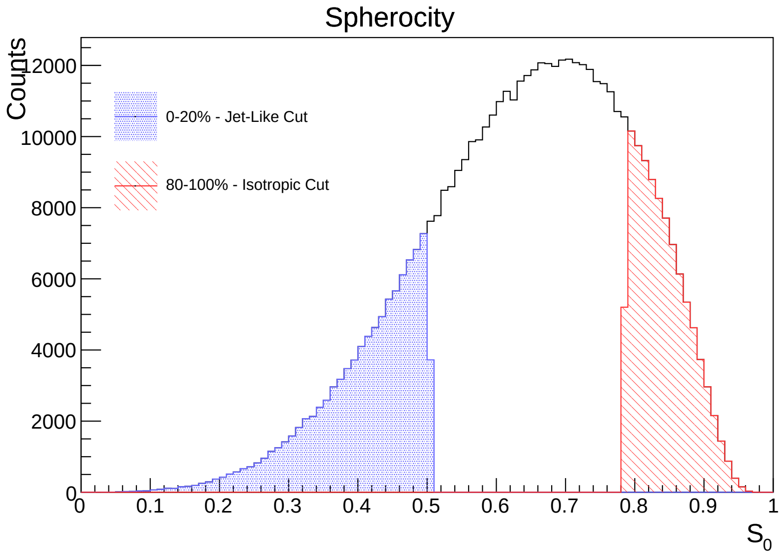

Figure 5.5: The spherocity distribution with the jet-like cut in blue and isotropic cut in red.

Table 4: Transverse Spherocity cuts for the different data sets.

	High Mult. [V0M]	**Jetty** [S_0]	**Isotropic** [S_0]
Default	69	0.505	0.785
Strange	68	0.505	0.785
Flow	79	0.515	0.795

5.3.2.2 Transverse Spherocity $p_T = 1$ This estimator works in exactly the same way as the Transverse Spherocity estimator mentioned above, except for all p_T being put to 1 in order to make it independent of momentum. Transverse Spherocity gives the same result if there was one parton with a specific momentum as if this one parton was divided into two partons with the same momentum direction but with half the momentum. One side effect from this is that if one track has a very high p_T compared to the rest, then this will dominate the spherocity calculation and make $S_0 \approx 0$ which means that it is very important if this one high p_T track is detected or not. Hence, by putting $p_T = 1$ for all particles there will be no momentum dependence and an event that would be jetty according to transverse spherocity, even though there is only one jetty track, will with this estimator be selected as an isotropic event.

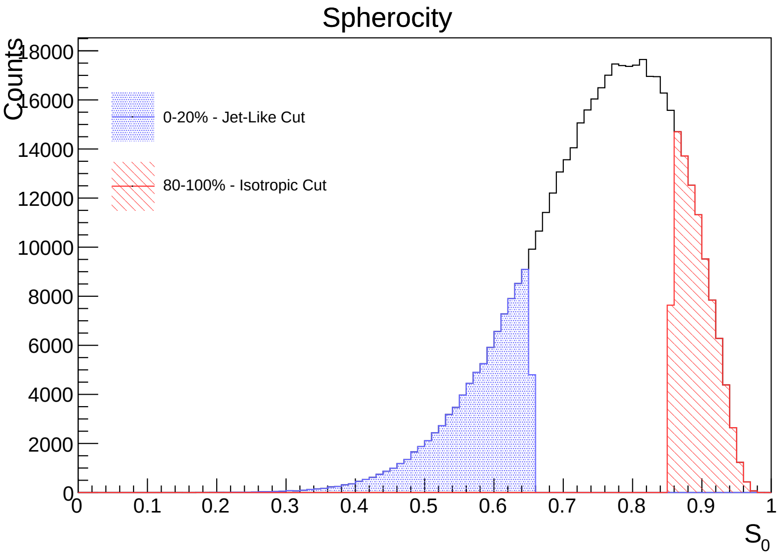

Figure 5.6: The altered spherocity distribution with the jet-like cut in blue and isotropic cut in red.

The same total distribution of all accepted events as a function of spherocity for this estimator is shown in Figure 5.6. As can be seen in both the distribution and the spherocity cuts in Table 5, the distribution is shifted more towards $S_0 = 1$ than the distribution with a p_T dependence in Figure 5.5.

5.3.2.3 The Mid-Forward estimator The Mid-Forward estimator was developed in hope to solve the problem of the anti-ridge found in the selected isotropic events using Transverse Spherocity. The idea behind it is to cut on multiplicity in different

Table 5: Selection cuts for the different data sets using Transverse Spherocity with $p_T = 1$

	High Mult.[V0M]	**Jetty** $[S_0]$	**Isotropic** $[S_0]$
Default	69	0.655	0.855
Strange	68	0.655	0.855
Flow	79	0.665	0.865

pseudorapidity regions; the mid-rapidity region and the forward rapidity region. This we hoped would give the advantage of not biasing on the ϕ-distribution which could result in larger radial and elliptic flow.

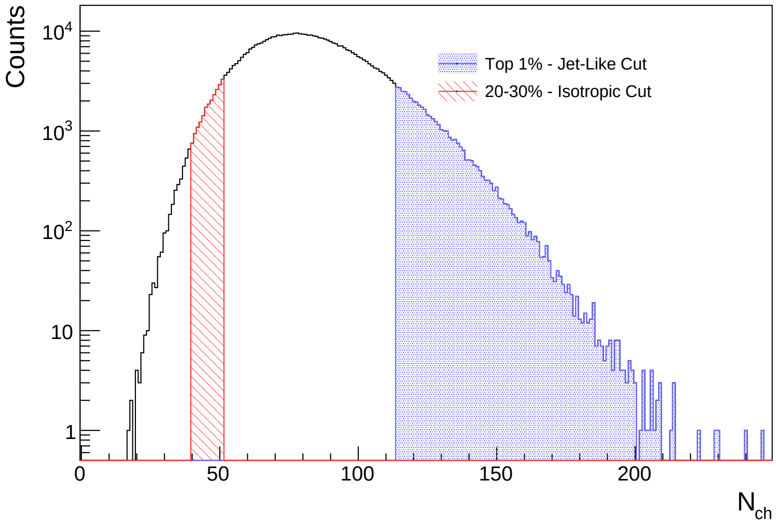

Figure 5.7: The number of charged particles (N_{ch}) multiplicity distribution after the top 10% cut done in V0M, with the isotropic cuts in red and jet-like cut in blue.

Just as the two previous described estimators, the Mid-Forward estimator cuts on the $0-10\%$ V0M multiplicity, this being in the forward rapidity region. The selection cuts were done in the mid-rapidity region, where the $0-1\%$ number of charged particles (N_{ch}) multiplicity were selected as jet-like events and the $20-30\%$ N_{ch} multiplicity were selected as isotropic events. Figure 5.7 shows the total event distribution as a function of N_{ch} multiplicity amplitudes. It also demonstrates the top 1% jet-like events in blur and $20-30\%$ isotropic events in red. In Table 6, the selection cuts for the different data sets are found.

5.3.3 Observables

In order to investigate how the different estimators perform, three different observable analyses were done in hope of finding one estimator that works well for all of them. These analyses will be discussed below.

Table 6: Selection cuts for the different data sets using the Mid-Forward estimator.

	High Mult.[V0M]	**Jet-Like** [N_{ch}]	**Isotropic** [N_{ch}]
Default	69	113	39-52
Strange	68	112	40-52
Flow	79	134	49-63

5.3.3.1 Elliptic Flow - Double Ridge The elliptic flow was measured using the two particle correlation analysis, explained in section 5.2, on the Default and Flow data-set. The pseudorapidity acceptance was put to $|\eta| < 2$ in order to get more statistics.

5.3.3.2 Radial Flow - Double Ratio For the study of radial flow the proton-to-pion double ratio (a ratio of two ratios) was analyzed, where the protons and pions were identified using their respective PDG codes. p_T spectra for the protons and pions were produced in the pseudorapidity range of $|\eta| < 0.8$. The p_T-spectrum for the proton was then divided by the pion p_T-spectrum. This ratio was performed for three different event selections; one with no event selection (minimum-bias), one with high multiplicity jet-like events and another with high multiplicity isotropic events. The jet-like and isotropic proton-to-pion ratios were then divided by the minimum-bias proton-to-pion ratio resulting in the double ratio. The idea is that protons are "shifted" to higher p_T by the flow, leading to a small suppression at low p_T and a somewhat larger enhancement at higher p_T (where there are less particles), see Figure 3.1.

5.3.3.3 Strangeness Enhancement A p_T-integrated strange particle yield to pion ratio as a function of V0M multiplicities measured in $|\eta| < 0.8$ was done for each data set as a check to see that the Strange data-set was properly created. These ratios were done, as in Figure 3.5, for K^0, $\Lambda + \bar{\Lambda}$, $\Xi + \bar{\Xi}$, and $\Omega^- + \bar{\Omega}^+$ and shown in Figure 5.8.

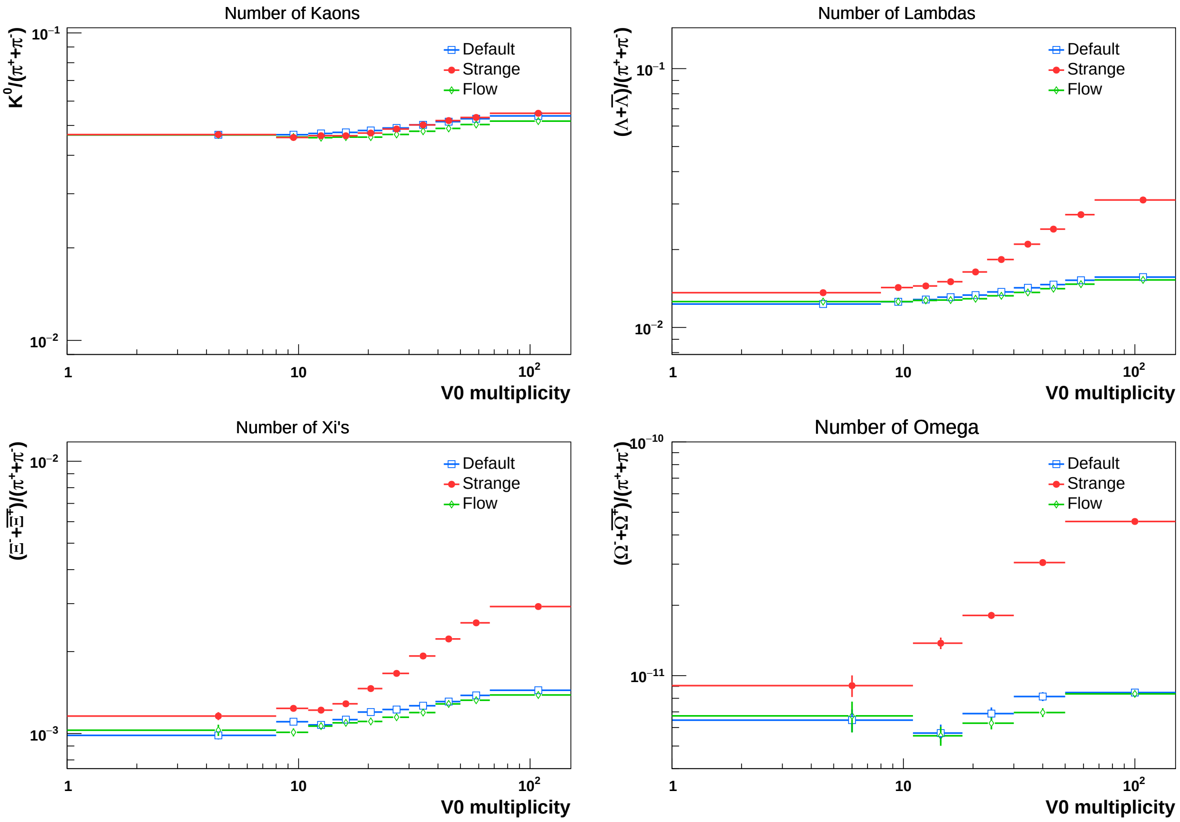

Figure 5.8: A comparison of strangeness enhancement for strange hadrons between the Default, Strange, and Flow data sets.

The analysis of the strangeness enhancement observable was only done on the Strange data-set using the Mid-Forward estimator. This analysis was performed in the same way as the radial flow analysis with the double ratio, but instead of a ratio of protons to pions, a ratio of strange hadrons; K^0, $\Lambda + \bar{\Lambda}$, $\Xi + \bar{\Xi}$, and $\Omega^- + \bar{\Omega}^+$, to pions was performed.

5.4 Data Analysis

5.4.1 Data Set and Event Selection

The data analysis in this thesis was performed using a data set with 125×10^6 events of pp collisions at $\sqrt{s} = 13$ TeV. It was recorded by the ALICE detector in 2016 at the LHC16k period. A basic event selection was done on this data set where the events had to pass some selection criteria. Pile-up events containing more than one collisions were rejected by requiring that for events with two primary vertices, will the SPD reconstructed vertex have to lie within 0.5 cm along the beam axis of the primary vertex reconstructed using tracks. Accepted events had to have at least one reconstructed track in the SPD that has a pseudorapidity range within $|\eta| < 1.0$. Events were also required to have a reconstructed vertex at a point that lies within 10 cm from the apparent interaction point.

5.4.2 Two Particle Correlations as a Function of the Mid-Forward estimator

A two particle correlations analysis (section 5.2) was done on the data set mentioned in previous section, using the Mid-Forward estimator. Only events within $|\eta| < 0.8$ were retained in order to assure full TPC acceptance. The selection cuts for the Mid-Forward estimator are shown in Table 7.

Table 7: Selection cuts on the LHC16k data set using the Mid-Forward estimator. The V0M multiplicity distribution for this data set was already presented in multiplicity classes of percent, hence the cut was done on the 10% bin.

	High Mult.[V0M]	**Jet-Like** $[N_{ch}]$	**Isotropic** $[N_{ch}]$
LHC16k data set	top 10%	47	14-19

6 Results and Discussion

6.1 PYTHIA Studies

6.1.1 Two Particle correlations

All the results in this section will show the associated yield per trigger particle in $\Delta\phi$ and $\Delta\eta$ for charged particle pairs with $2 < p_{T,trig} < 4$ GeV/c and $1 < p_{T,assoc} < 2$ GeV/c in simulated pp collisions at $\sqrt{s} = 13$ TeV. The two particle correlations measurements done on the Default data-set will be presented first, followed by measurements done on the Flow data-set.

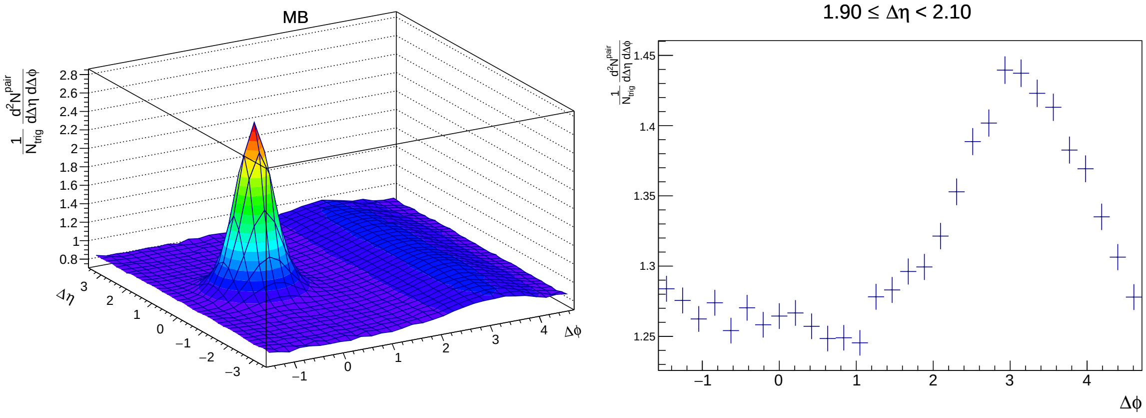

(a) (b)

Figure 6.1: (a) shows the corrected signal distribution for high multiplicity events using the *Default* data-set. (b) shows a projection of the signal distribution in $\Delta\phi$ away from the correlation peak in the region of $1.90 \leq \Delta\eta \leq 2.10$.

6.1.1.1 Default Data-Set In Figure 6.1 the corrected signal distribution for high multiplicity events is shown together with its projection. Some visible features in (a) are the correlation peak close to $(\Delta\phi, \Delta\eta) \approx (0, 0)$, and the elongated structure, the "ridge", at $\Delta\phi \approx \pi$. The distribution in $\Delta\phi$ in (b) is more or less flat between $-\pi/2$ and $\pi/2$, and the away side peak is more clearly seen at $\Delta\phi \approx \pi$, which was expected since there is no flow in the Default data-set.

Figure 6.2 shows the corrected signal distributions for high multiplicity jet-like events, where the jet-like events were selected using the different estimators. In (a) and (b) the transverse spherocity estimator was used and except for the away side peak at $\Delta\phi \approx \pi$ in (b), there is an irregular bump around $\Delta\phi \approx 0$. The altered spherocity estimator, where all p_T were put to 1, was used for (c) and (d), and the irregular bump seen in (b) is also seen in (d). This bump is, however, not seen in (f) where the mid-forward estimator was used for selecting jet-like events. This suggests that the mid-forward selection, unlike the spherocity estimators, does not introduce a strong azimuthal bias.

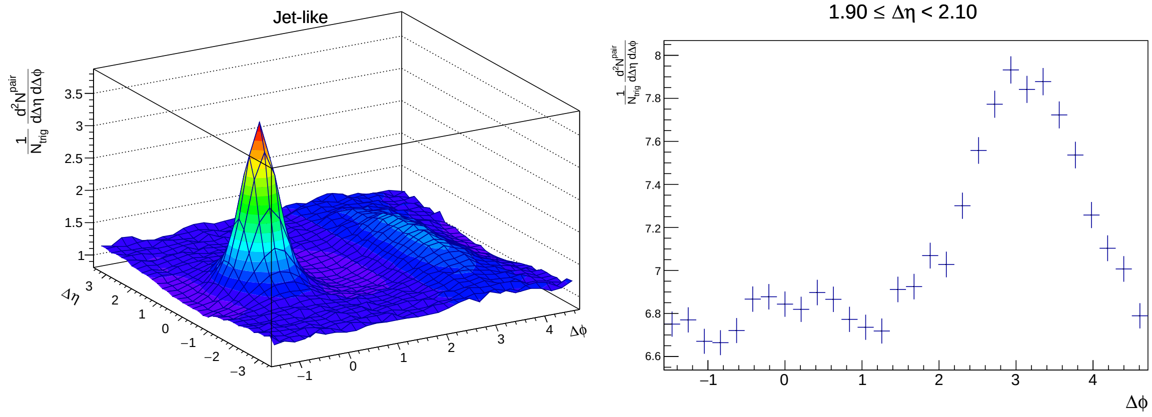

(a) Spherocity (b) Spherocity

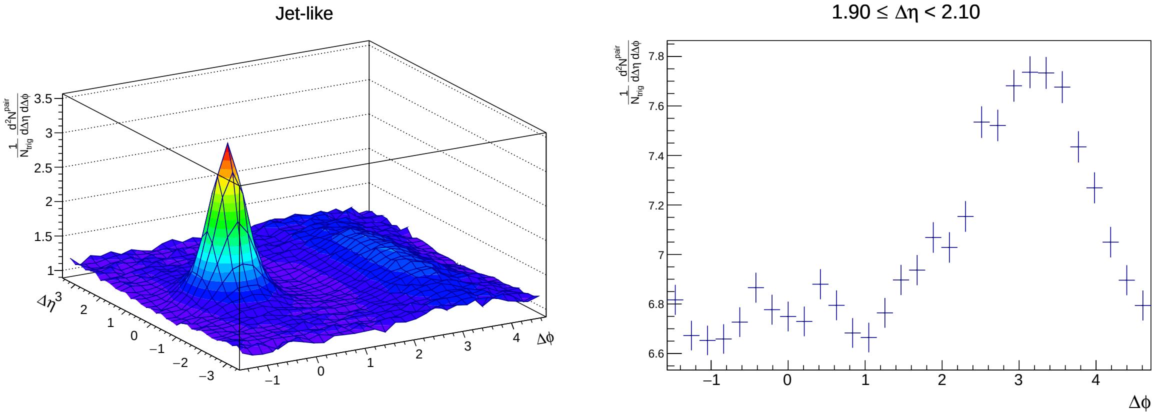

(c) Spherocity pt =1 (d) spherocity pt=1

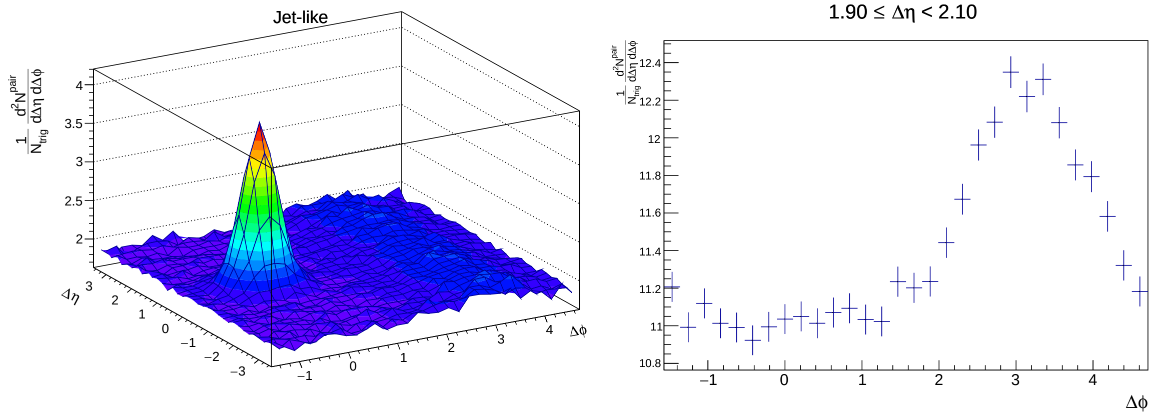

(e) Mid-Forward (f) Mid-Forward

Figure 6.2: The figures to the left show the corrected signal distribution for high multiplicity *jet-like* events using the three different estimators on the *Default* data-set, while the figures to the right shows the projections of the signal distributions in $\Delta\phi$ away from the correlation peak in the region of $1.90 \leq \Delta\eta \leq 2.10$.

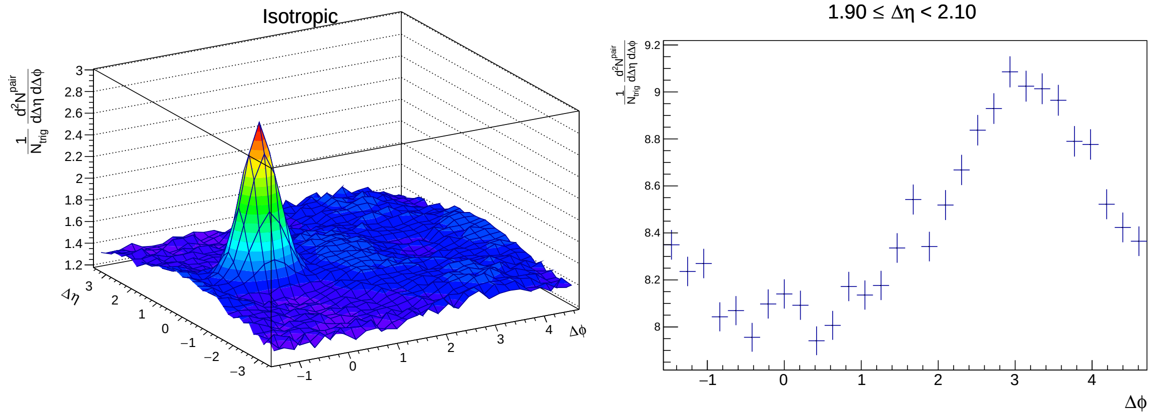

(a) Spherocity (b) Spherocity

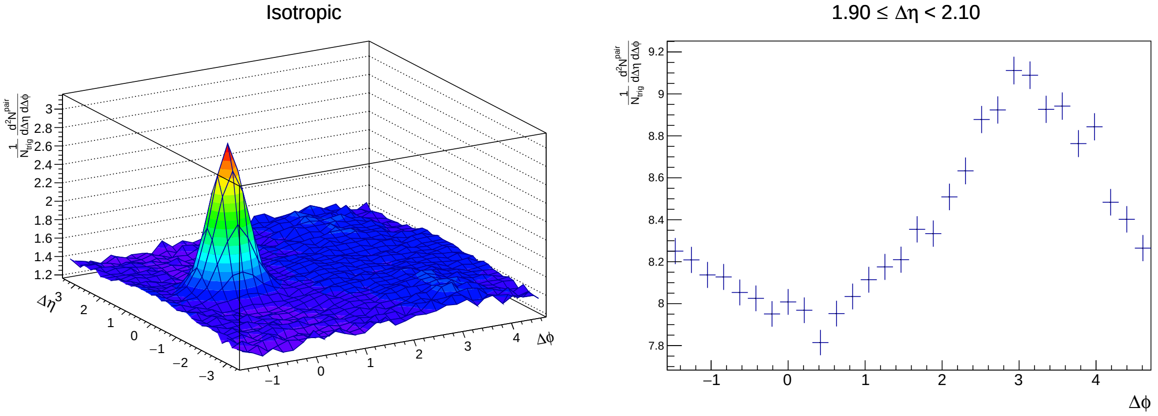

(c) Spherocity Pt = 1 (d) Spherocity pt = 1

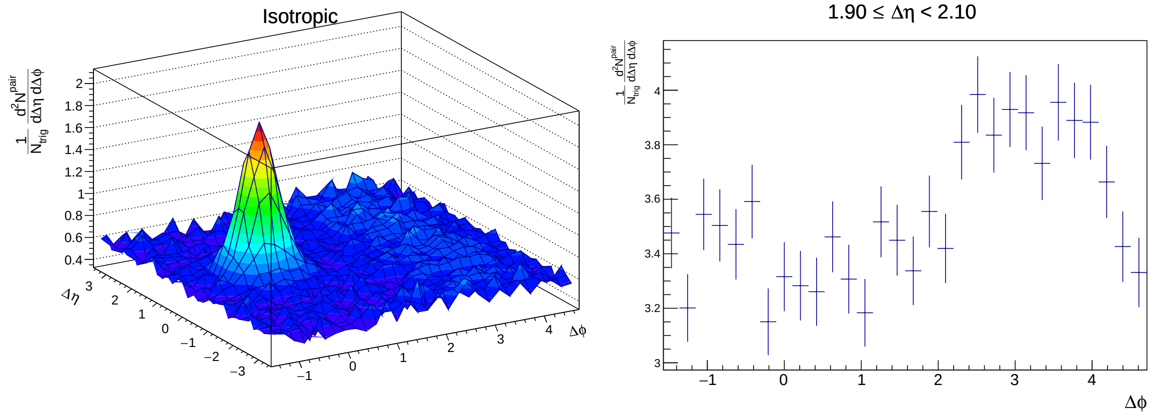

(e) Mid-Forward (f) Mid-Forward

Figure 6.3: The figures to the left show the corrected signal signal distribution for high multiplicity *isotropic* events using the three different estimators on the *Default* data-set, while the figures to the right shows the projections of the signal distributions in $\Delta\phi$ away from the correction peak in the region of $1.90 \leq \Delta\eta \leq 2.10$.

Figure 6.3 shows the corrected signal distribution for high multiplicity isotropic events and just as in Figure 6.2, 6.3 shows how the different estimators performed. The spherocity selected isotropic events in (a) and (b) looks somewhat different from the unbiased high multiplicity events in Figure 6.1 and the jet-like events in Figure 6.2. The away-side peak in (b) is broader, and there is a dip in the near-side region which comes from the spherocity bias. This is also seen in (d) except for that the very small bump is not as distinct here. In (e) and (f) the mid-forward estimator was used, where the away-side ridge is more distinguishable in (e) than in (a) and (c) which is also seen in (f).

From the results using the Default data set, it seems as if the performance of the two different transverse spherocity estimators were somewhat similar. The irregular bump in the near-side region of the jet-like events could be a near-side ridge, which was not expected. Does this mean that flow-like behaviour is an initial state effect or is it due to that the estimators do not perform very well when selecting the jet-like events? As for the isotropic events using the transverse spherocity estimators, the results do not look as expected. In fact, by studying different η ranges, it gets clear that there is no distinguishable away-side ridge even though it appears to be one in the η range given in Figure 6.3. In the $\Delta\eta$ range of $0.10 < \Delta\eta < 0.30$ shown in Figure 6.4, the original transverse spherocity estimator in (a) gives a signal distribution in $\Delta\phi$ that appears as an anti-ridge with the correlated jet-peak at $\Delta\phi = 0$. This agrees with the results in [2] where the two particle correlations were applied on real data with restrictions in the $\Delta\eta$ due to detector acceptance. The anti-ridge is not seen at all in (b) where the transverse spherocity estimator with all p_T put to one was used. However, the away-side ridge, which was expected to be seen, is not seen either, and it seems as if both the transverse spherocity and transverse spherocity where all p_T is put to one estimator has a bias in ϕ. The mid-forward estimator was developed in a try to avoid this bias in ϕ. The results of using the mid-forward estimator agrees more with how the jet-like and isotropic events was expected to look like for the Default data-set, even though it is hard to tell if there is a near-side ridge for isotropic events, at least there is no anti-ridge.

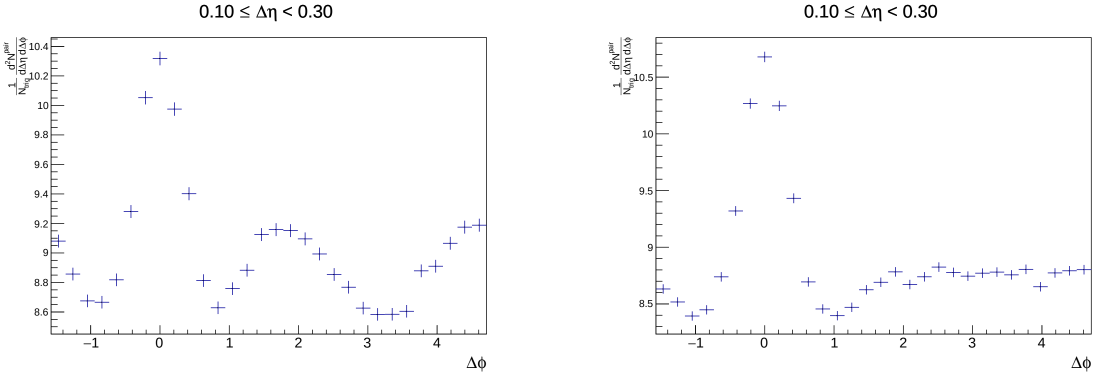

(a) Spherocity

(b) Spherocity $p_T = 1$

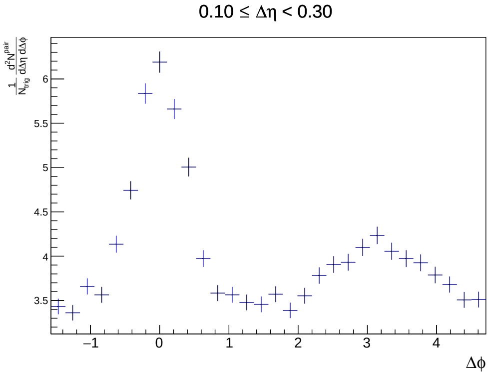

(c) Mid-Forward

Figure 6.4: The projections of the corrected signal distribution for high multiplicity *isotropic* events using the *Default* data-set in $\Delta\phi$ in the region of $0.1 \leq \Delta\eta \leq 0.3$.

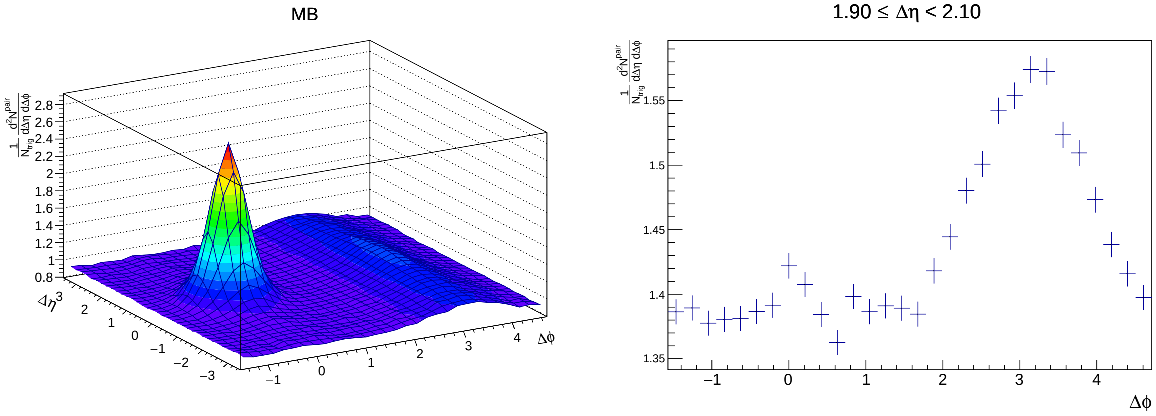

(a) (b)

Figure 6.5: (a) shows the corrected signal signal distribution for high multiplicity events using the *Flow* data-set. (b) shows a projection of the signal distribution in $\Delta\phi$ away from the correction peak in the region of $1.90 \leq \Delta\eta \leq 2.10$.

6.1.1.2 Flow Data-Set Figure 6.5 shows the corrected signal distribution for high multiplicity events, but this time using the *Flow* data-set. As in Figure 6.1, some visible features in (a) are the correlation peak close to $(\Delta\phi, \Delta\eta) \approx (0, 0)$, and the elongated structure, the "ridge", at $\Delta\phi \approx \pi$. However, the projection of the signal distribution shown in (b), shows the additional near-side ridge at $\Delta\phi = 0$, which was expected since there is flow in this data-set.

As in Figure 6.2, Figure 6.6 shows the corrected signal distribution for high multiplicity jet-like events, where the jet-like events were selected using the different estimators. The projections in (b) and (d) using the transverse spherocity and the altered transverse spherocity estimator respectively, both show a somewhat more distinct double ridge than in Figure 6.2. For an optimal estimator, the jet-like events would likely not show collective behaviour even though there is flow in the system since the goal is to only select events dominated by hard scatterings, i.e. no collective behaviour. With this in mind, the jet-like events selected using the mid-forward estimator achieve a better result, although there could be a near-side peak at $\Delta\phi = 0$.

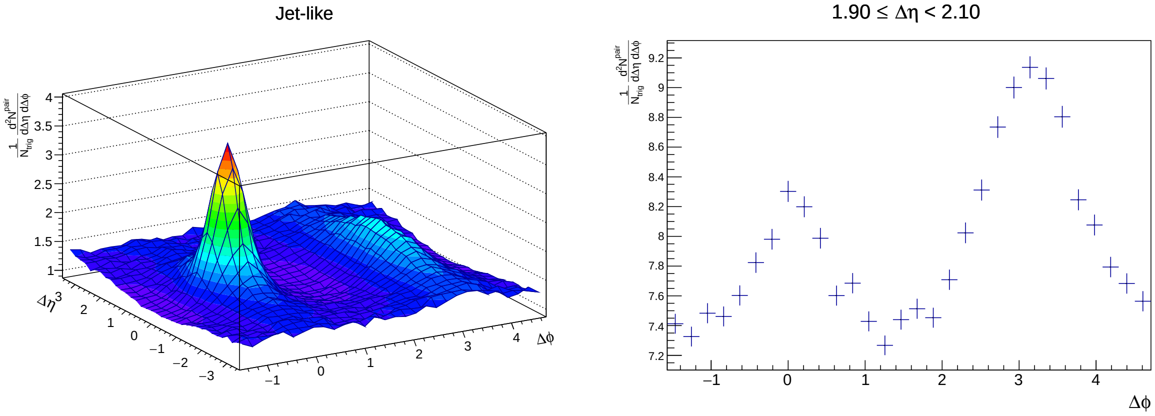

(a) Spherocity (b) Spherocity

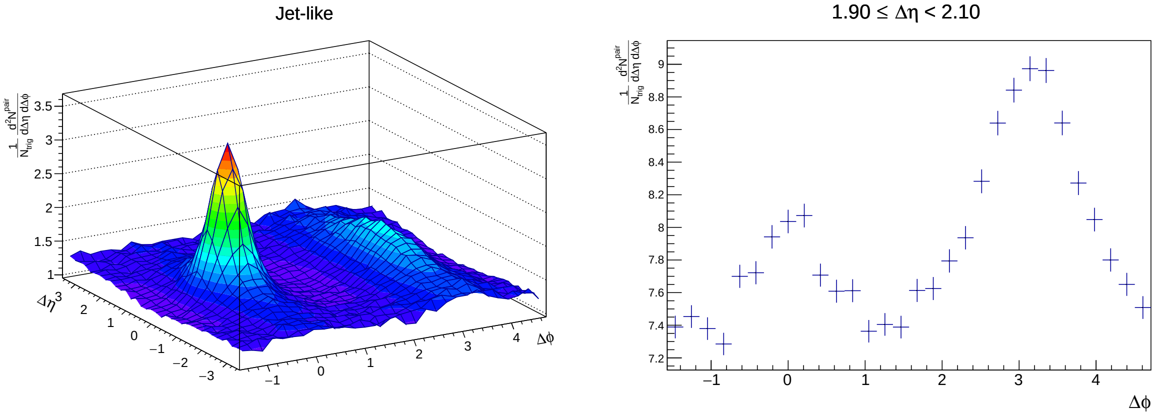

(c) Spherocity $p_T = 1$ (d) Spherocity $p_T = 1$

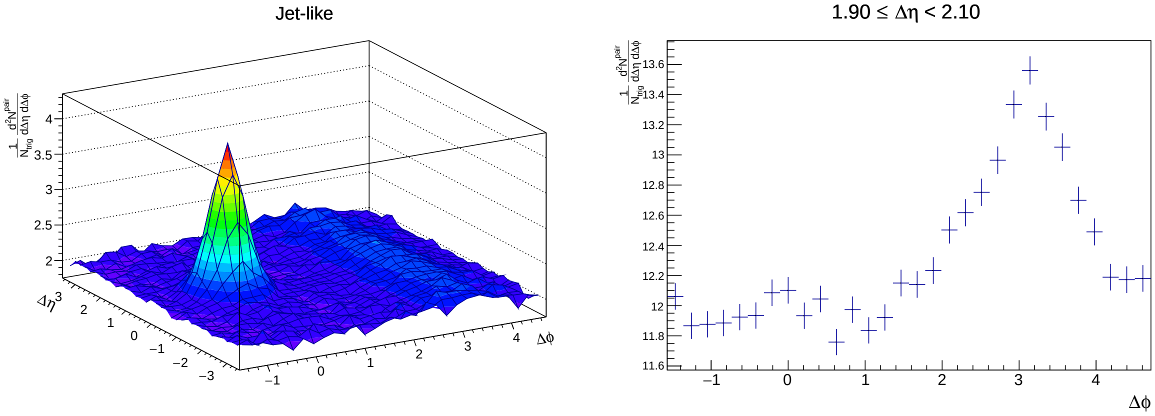

(e) Mid-Forward (f) Mid-Forward

Figure 6.6: The figures to the left show the corrected signal signal distribution for high multiplicity *jet-like* events using the three different estimators on the *Flow* data-set, while the figures to the right shows the projections of the signal distributions in $\Delta\phi$ away from the correction peak in the region of $1.90 \leq \Delta\eta \leq 2.10$.

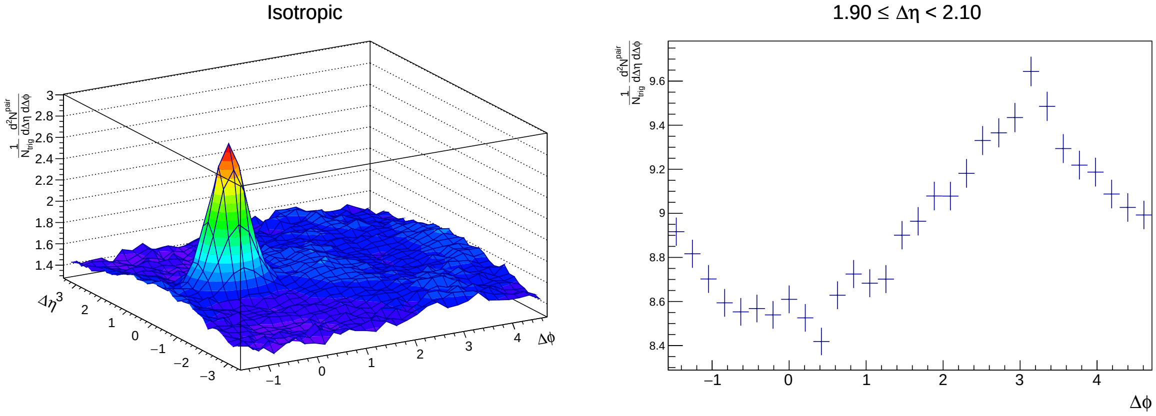

(a) Spherocity (b) Spherocity

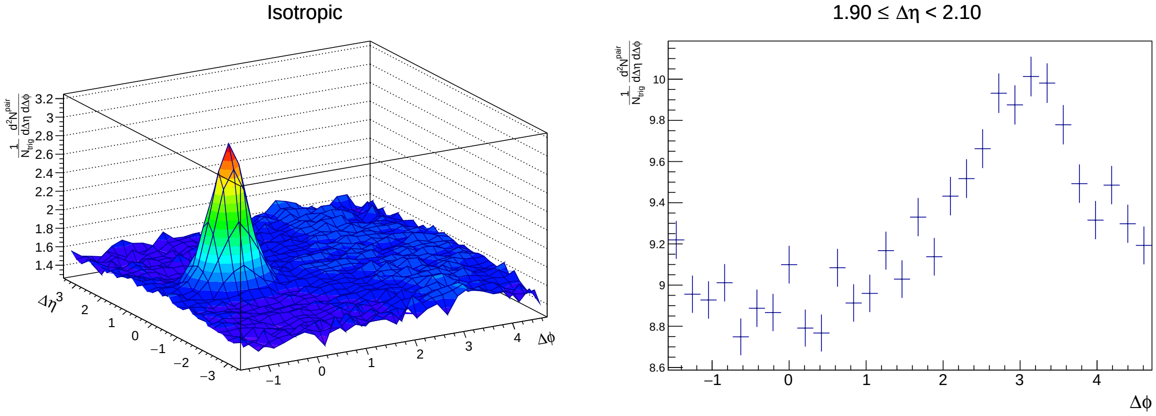

(c) Spherocity $p_T = 1$ (d) Spherocity $p_T = 1$

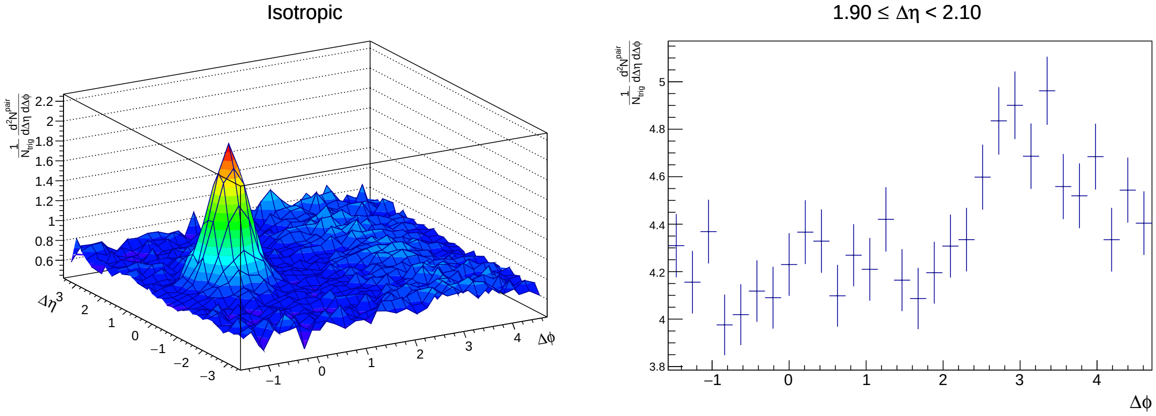

(e) Mid-Forward (f) Mid-Forward

Figure 6.7: The figures to the left show the corrected signal signal distribution for high multiplicity *isotropic* events using the three different estimators on the *Flow* data-set, while the figures to the right shows the projections of the signal distributions in $\Delta\phi$ away from the correction peak in the region of $1.90 \leq \Delta\eta \leq 2.10$.

The results of the corrected signal distribution for isotropic events in Figure 6.7, where the Flow data-set was used, show similar features as in Figure 6.3. The projections where the transverse spherocity estimators, (b) and (d), were used, still show signs of a bias in ϕ, while it looks as if there could be a double ridge for the isotropic selected events using the mid-forward estimator. Based on all the results presented up til now, the mid-forward estimator was selected as the estimator to use for the strangeness enhancement and the real data analysis.

6.1.2 Radial Flow - Double Ratio

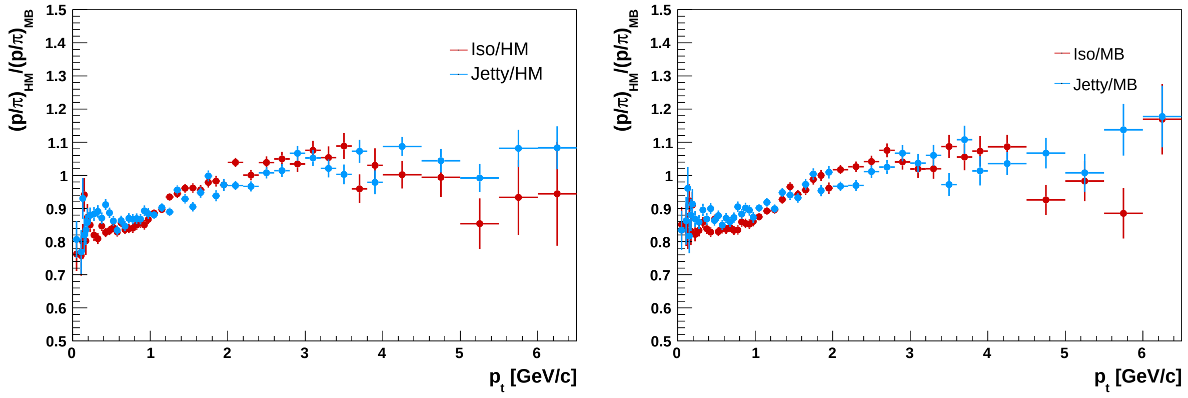

(a) Spherocity

(b) Spherocity $p_T = 1$

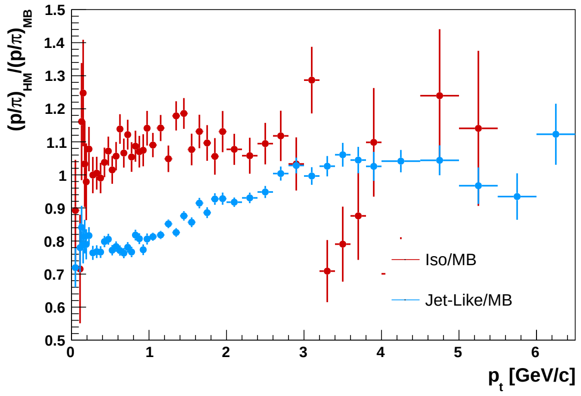

(c) Mid-Forward

Figure 6.8: The proton-to-pion double ratio using the three different estimators on the *Default* data-set.

Figure 6.8 shows double proton-to-pion ratios as a function of p_T using the different estimators on the *Default* data-set. In (a) the transverse spherocity estimator was used in order to separate the high multiplicity events into jet-like and isotropic events. An enhancement of jet-like events is observed for $p_T < 1$ GeV/c, while in intermediate p_T a small isotropic enhancement is observed. The p_T-independent transverse spherocity estimator was used in (b) where the same phenomena as in (a) is observed. In (c) where the mid-forward estimator was used, an enhancement of isotropic events is observed for $p_T < 3$ GeV/c.

The easiest way to understand the double ratio is to look at Fig. 3.1 and 3.2. The radial flow will "shift" particles to higher p_T and the effect is larger for heavier particles. This means that we expect the double ratio to decrease (increase) at low (intermediate) p_T when the radial flow grows. This is also what we observe in Fig. 6.8 (a) and (b) but there the effect is known to be caused by Color Reconnection (CR) [44]. CR is an effect implemented in PYTHIA in which the strings from two or more hard scatterings are reconnected to reduce the number of strings. It mimics radial flow but does not require a medium.

In the Default data-set no extra model is "switched" on, hence only a small effect of CR mimicking radial flow is expected. The results in (a) and (b) agrees with these expectations, meaning that both transverse spherocity estimators performed as predicted. Regarding the mid-forward estimator, where an isotropic enhancement is observed, it seems as if one might select events to be isotropic even if they are not.

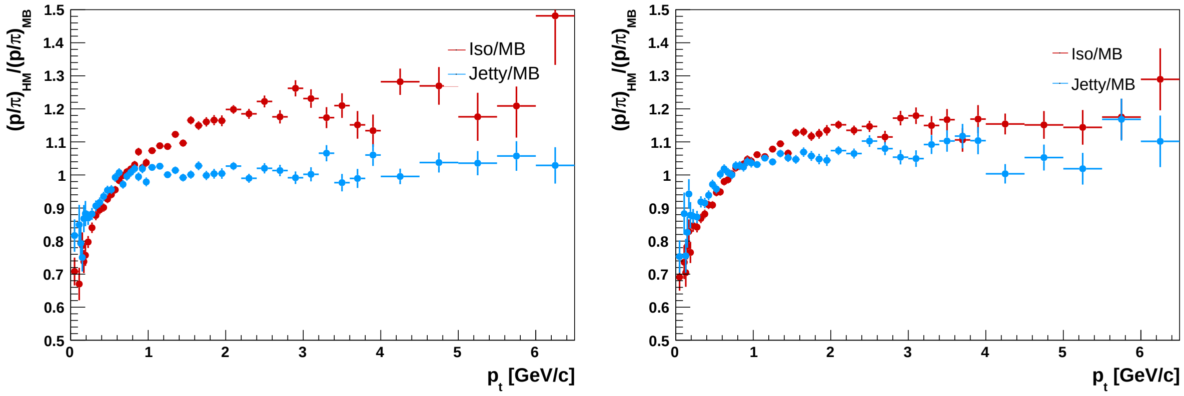

(a) Spherocity

(b) Spherocity $p_T = 1$

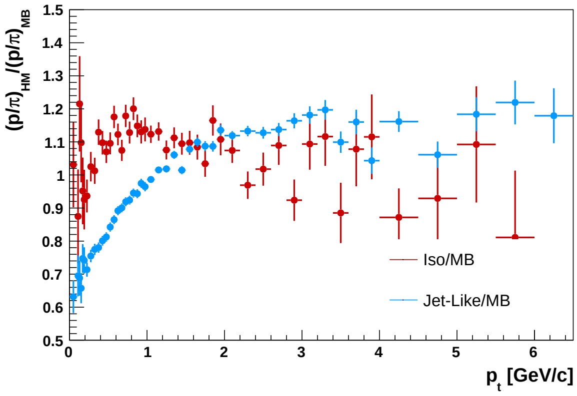

(c) Mid-Forward

Figure 6.9: The proton-to-pion double ratio using the three different estimators on the *Strange* data set.

Figure 6.9 shows double proton-to-pion ratios as a function of p_T using the different estimators, but this time on the *Strange* data-set. In (a) the transverse spherocity estimator was used. The jet-like events are still enhanced at $p_T \lesssim 1$ GeV/c, however, at $p_T > 1$ GeV/c the isotropic events are enhanced while the jet-like events are suppressed. This is also observed in (b), where the p_T-independent transverse spherocity estimator is used, although the jet-like events are not as suppressed as in (a). In (c) an enhancement of isotropic events is observed for $p_T \lesssim 1.6$ GeV/c, above this value it is suppressed and the jet-like events are enhanced.

The larger strange-quark production in the Strange data-set seem to give a larger CR effect when using the spherocity estimators. The results from using the mid-forward estimator shows somewhat the opposite from what was expected for radial flow. From these results it looks as if the spherocity estimators still works well for the radial flow observable while the mid-forward estimator does not.

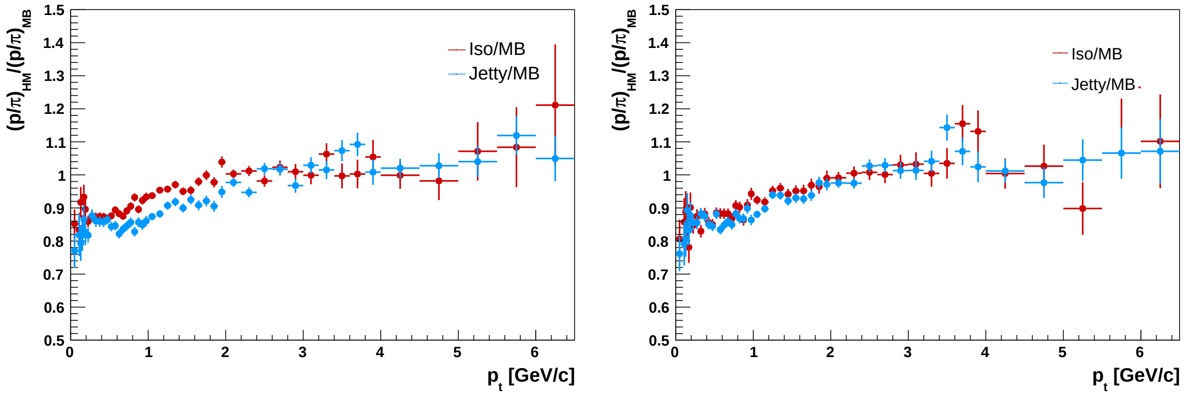

(a) Spherocity (b) Spherocity $p_T = 1$

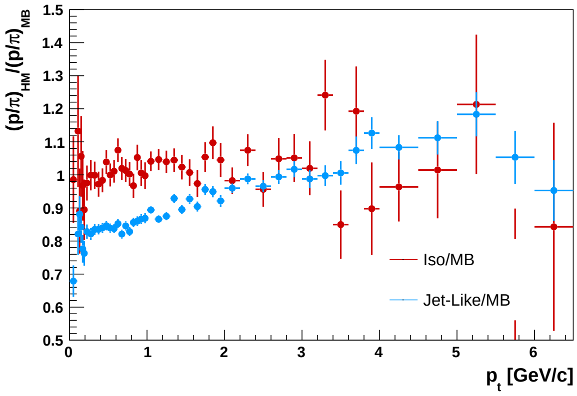

(c) Mid-Forward

Figure 6.10: The proton-to-pion double ratio using the three different estimators on the *Flow* data set.

The Flow data-set was used for the double proton-to-pion ratio in Figure 6.10. In (a) the isotropic events are enhanced in $0.5 \lesssim p_T \lesssim 2$ when using the transverse spherocity estimator, while a very small enhancement of isotropic events is observed in (b) where the p_T-independent transverse spherocity estimator was used. In (c) the isotropic events are enhanced up to $p_T \approx 2$ GeV/c. Above this value it is hard to determine what is enhanced and what is suppressed.

In the Flow data-set, string shoving is "switched" on and an enhancement of isotropic events at intermediate p_T is expected and an even bigger enhancement than in Figure 6.8 and 6.9. In fact there is a larger enhancement of isotropic events in Figure 6.10 (a) than in Figure 6.8 (a), but not as large as in Figure 6.9 (a). However, the results for the proton-to-pion double ratio using the transverse spherocity estimator on the Flow data-set agrees better with results of radial flow presented in [44], than with the same estimator used on the Strange data-set. The results using the altered transverse spherocity estimator on the Flow data-set does not seem to work very well for radial flow since it is hard to see an enhancement or suppression of isotropic events. The mid-forward estimator still does not work well for radial flow.

6.1.3 Strangeness Enhancement

The goal here was to do a strangeness enhancement analysis using the mid-forward estimator. Unfortunately there was no time to finish the full analysis. Hence, the unfinished results are presented below.

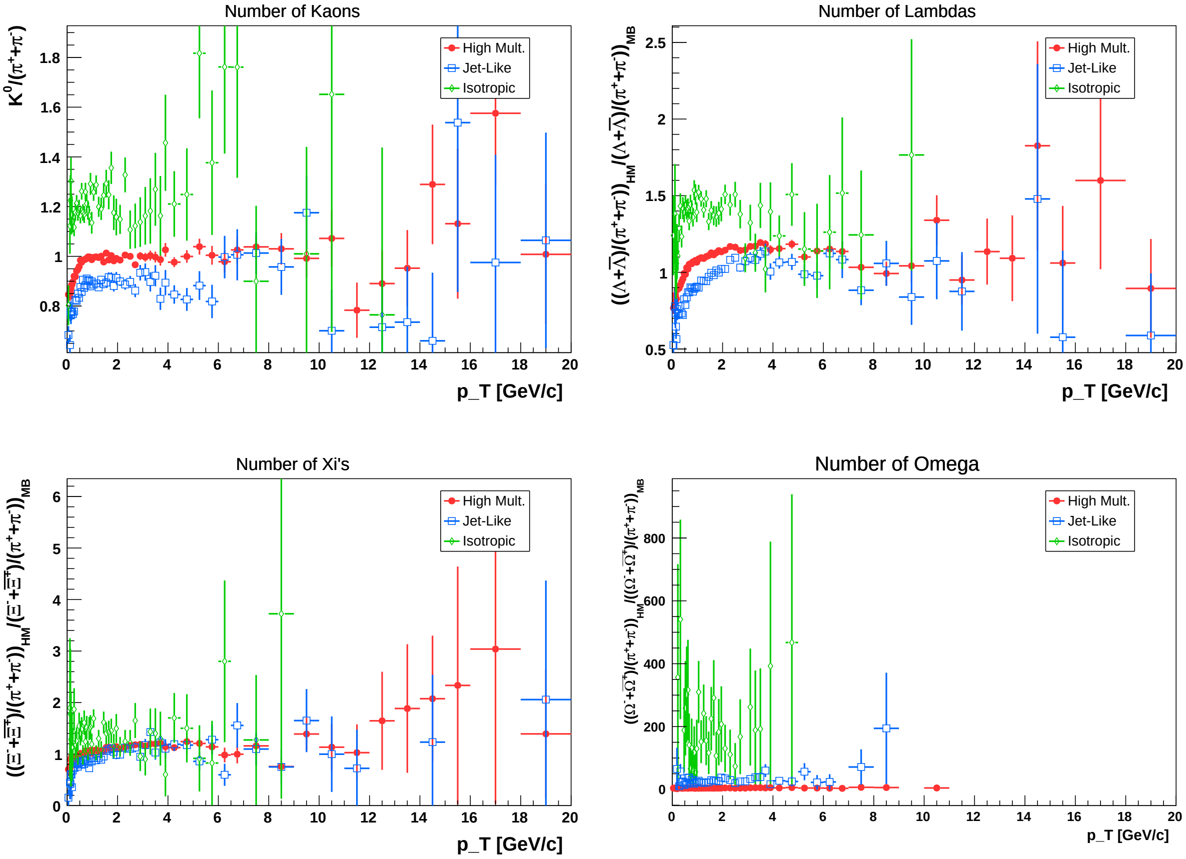

Figure 6.11: The strange-hadron-to-pion double ratio using the Mid-Forward estimator as a function of p_T.

The isotropic events are expected to be enhanced due to the strange-quark production in a possibly produced strongly interacting medium. This enhancement is observed for all strange-hadrons even though it is hard to tell because of the very large error bars. The rest of the phenomena have to be further looked into.

6.2 Data Analysis

The mid-forward estimator was chosen to be tested on ALICE data because of its slightly better performance in the simulation studies when analysing the double ridge. This section will show the associated yield per trigger particle in $\Delta\phi$ and $\Delta\eta$ for charged particle pairs with $2 < p_{T,trig} < 4$ GeV/c and $1 < p_{T,assoc} < 2$ GeV/c in pp collisions at $\sqrt{s} = 13$ TeV recorded by the ALICE detector. The two particle correlation measurements for high multiplicity events will be presented first, followed by the same measurements done for jet-like and isotropic events.

6.2.1 Two Particle Correlations as a function of the Mid-Forward Estimator

In Figure 6.12 the corrected signal distribution for high multiplicity events is shown together with its projection. The visible features in (a) are the correlation peak at

$(\Delta\phi, \Delta\eta) \approx (0, 0)$ and the away side ridge at $\Delta\phi \approx \pi$. It is hard to tell if there is a ridge at $\Delta\phi \approx 0$. In (b), however, there is a small indication of a double ridge.

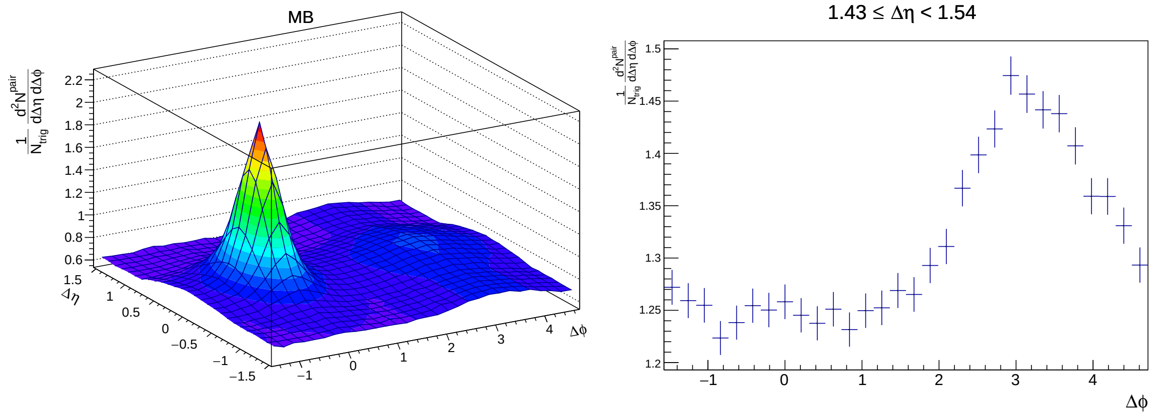

(a) (b)

Figure 6.12: (a) shows the corrected signal distribution for high multiplicity events in pp collisions at $\sqrt{s} = 13$ TeV. (b) shows a projection of the signal distribution in $\Delta\phi$ away from the correction peak in the region of $1.43 \leq \Delta\eta \leq 1.54$.

Figures 6.13 and 6.14 show the corrected signal distributions for high-multiplicity jet-like and isotropic events, respectively, in (a), and their projections in (b). The correlation peak and away side bridge are visible in both jet-like and isotropic events. In the projections it seems as if the jet-like events give a double ridge with a near-side ridge shifted closer to the away-side ridge, while the isotropic events show a more even distribution where it is hard to tell if there is a double ridge due to the low statistics.

These results do not agree with the results from the simulation study. The jet-like projection distribution in Figure 6.13 is more similar to the simulated isotropic projection distribution, which was not expected. The disagreement in the results indicates that the mid-forward estimator works differently in simulations compared to data.

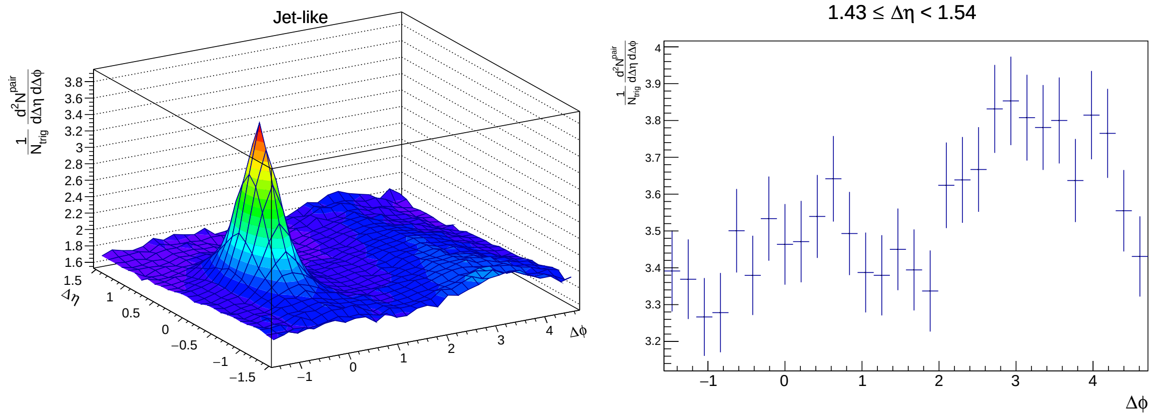

(a) (b)

Figure 6.13: (a) shows the corrected signal distribution for high multiplicity *jet-like* events in pp collisions at $\sqrt{s} = 13$ TeV. (b) shows a projection of the signal distribution in $\Delta\phi$ away from the correction peak in the region of $1.43 \leq \Delta\eta \leq 1.54$.

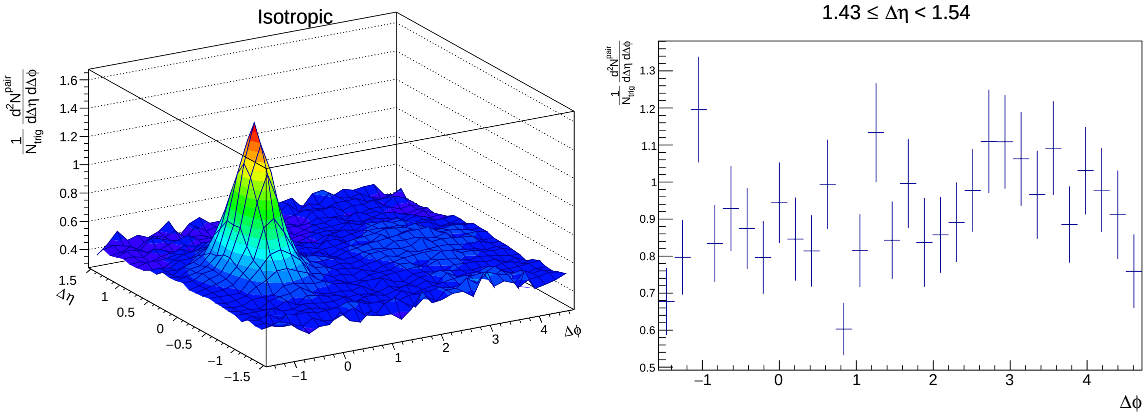

(a) (b)

Figure 6.14: (a) shows the corrected signal distribution for high multiplicity *isotropic* events in pp collisions at $\sqrt{s} = 13$ TeV. (b) shows a projection of the signal distribution in $\Delta\phi$ away from the correction peak in the region of $1.43 \leq \Delta\eta \leq 1.54$.

7 Conclusion and Outlook

The goal for this thesis work was to study different possible QGP estimators in order to find an estimator that works for more than one QGP observable. The first part of the project involved simulation studies where three different estimators were tested on three different data-sets looking at three different observables. The different estimators that were investigated were Transverse Spherocity, an altered version of Transverse Spherocity where all p_T were put to one, and a new technique called the Mid-Forward estimator where measurements from mid and forward pseudorapidity ranges are combined. The simulated data-sets were produced using the Monte Carlo event generator called PYTHIA that has new microscopic models included. For two of the produced data-sets the Rope Hadronization framework were used; one had string shoving switched on and the other used the rope hadronization model. The third data-set used no extra model. The idea of this project started from the observation made in [2] where the two particle correlation method as a function of transverse spherocity estimator was studied, hence, one of the observables that was used to test the estimators was the elliptic flow (the double ridge). The other two observables were radial flow and strangeness enhancement.

The results from the simulation study on radial flow, once again confirmed that the transverse spherocity estimator performs well for radial flow. For the altered spherocity estimator the difference between jet-like and isotropic events was not as clear, however, the results still agreed with the predictions. The mid-forward estimator did not perform too well for the radial flow observable if the expected results should agree with [15, 44]. Results from the two particle correlation method using the two spherocity estimators agreed with the observation made in [2] where a bias in $\Delta\phi$ is observed for isotropic events was seen. Hence, they did not work well for the elliptic flow observable. The bias in $\Delta\phi$ does not appear using the mid-forward estimator and the results of the jet-like and isotropic events does somewhat agree with predictions, making this estimator the best candidate for the elliptic flow observable. Since the analysis of strangeness enhancement was not finished it is hard to make a conclusion from these results. As a general conclusion of the results from the simulation studies, none of the tested estimators worked for more than one observable.

For the second part of this project a data analysis was done where the elliptic flow was measured using two particle correlations as a function of the mid-forward estimator. The mid-forward estimator was chosen due to is being the best candidate for elliptic flow. These results did not agree with the simulated results, but this might be improved with more statistics.

An obvious continuation of this project is to finish the strangeness enhancement analysis. In addition to this it would be interesting to fine tune the multiplicity cuts for the mid-forward estimator in order to gain more understanding of the estimator. It would also be interesting to try the mid-forward estimator on the other observables (radial flow and strangeness enhancement) on real data to see if these results agree with the results from the simulation studies.

Appendix A

Rope Hadronization Details

Pythia 8240

Vanilla:

```
pythia.readString(”SoftQCD:nonDiffractive = on”);
pythia.readString(”ParticleDecays:limitTau0 = on”);
pythia.readString(”ParticleDecays:tau0Max = 10”);
pythia.readString(”Random:setSeed = on”);
pythia.readString(”Random:seed = 0”);
```

Ridge:

```
pythia.readString(”ParticleDecays:limitTau0 = on”);
pythia.readString(”ParticleDecays:tau0Max = 10”);
pythia.readString(”Random:setSeed = on”);
pythia.readString(”Random:seed = 0”);

// Enabling flavour ropes, setting model parameters.
// The model is still untuned. These parameter values
// are choosen for illustrative purposes.
pythia.readString(”Ropewalk:RopeHadronization = on”);
pythia.readString(”Ropewalk:doShoving = on”);
pythia.readString(”Ropewalk:doFlavour = off”);
pythia.readString(”Ropewalk:rCutOff = 10.0”);
pythia.readString(”Ropewalk:limitMom = on”);
pythia.readString(”Ropewalk:pTcut = 2.0”);
pythia.readString(”Ropewalk:r0 = 0.41”);
pythia.readString(”Ropewalk:m0 = 0.2”);
pythia.readString(”Ropewalk:gAmplitude = 10.0”);
pythia.readString(”Ropewalk:gExponent = 1.0”);
pythia.readString(”Ropewalk:deltat = 0.1”);
pythia.readString(”Ropewalk:tShove = 1.”);
pythia.readString(”Ropewalk:deltay = 0.1”);
pythia.readString(”Ropewalk:tInit = 1.5”);

// Enabling setting of vertex information.
pythia.readString(”PartonVertex:setVertex = on”);
```

```
pythia.readString(”PartonVertex:protonRadius = 0.7”);
pythia.readString(”PartonVertex:emissionWidth = 0.1”);

pythia.init();
```

Strange:

```
//Prevent unstable particles from decaying
pythia.readString(”ParticleDecays:limitTau0 = on”);
pythia.readString(”ParticleDecays:tau0Max = 10”);
pythia.readString(”Random:setSeed = on”);
pythia.readString(”Random:seed = 0”);

//QCD based CR
pythia.readString(”MultiPartonInteractions:pT0Ref = 2.15”);
pythia.readString(”BeamRemnants:remnantMode = 1”);
pythia.readString(”BeamRemnants:saturation = 5”);
pythia.readString(”ColourReconnection:mode = 1”);
pythia.readString(”ColourReconnection:allowDoubleJunRem = off”);
pythia.readString(”ColourReconnection:m0 = 0.3”);
pythia.readString(”ColourReconnection:allowJunctions = on”);
pythia.readString(”ColourReconnection:junctionCorrection = 1.2”);
pythia.readString(”ColourReconnection:timeDilationMode = 2”);
pythia.readString(”ColourReconnection:timeDilationPar = 0.18”);

pythia.readString(”Ropewalk:RopeHadronization = on”);

pythia.readString(”Ropewalk:doShoving = on”);
pythia.readString(”Ropewalk:tInit = 1.5”); // Propagation time
pythia.readString(”Ropewalk:deltat = 0.05”);
pythia.readString(”Ropewalk:tShove 0.1”);
pythia.readString(”Ropewalk:gAmplitude = 0.”); // Set shoving strength to 0 explicitly

pythia.readString(”Ropewalk:doFlavour = on”);
pythia.readString(”Ropewalk:r0 = 0.5”);
pythia.readString(”Ropewalk:m0 = 0.2”);
pythia.readString(”Ropewalk:beta = 0.1”);

// Enabling setting of vertex information.
pythia.readString(”PartonVertex:setVertex = on”);
pythia.readString(”PartonVertex:protonRadius = 0.7”);
pythia.readString(”PartonVertex:emissionWidth = 0.1”);

pythia.init();
```

Bibliography

[1] Thomson M. Modern particle physics. New York: Cambridge University Press; 2013. Available from: `http://www-spires.fnal.gov/spires/find/books/www?cl=QC793.2.T46::2013`.

[2] Staaden M. An attempt to isolate the double ridge in high multiplicity pp collisions using the transverse spherocity; 2018. Student Paper.

[3] Martin BR, Shaw G. Particle Physics. Manchester Physics Series. Wiley; 2008.

[4] Mårtenson M. Strange Hadron Production as a Function of Multiplicity and Transverse Spherocity in proton-proton Collisions at $\sqrt{s} = 13$ TeV; 2018. Student Paper.

[5] Tanabashi M, Hagiwara K, Hikasa K, Nakamura K, Sumino Y, Takahashi F, et al. Review of Particle Physics. Phys Rev D. 2018 Aug;98:030001. Available from: `https://link.aps.org/doi/10.1103/PhysRevD.98.030001`.

[6] Florkowski W. Phenomenology of Ultra-Relativistic Heavy-Ion Collisions; 2010.

[7] Kane GL. MODERN ELEMENTARY PARTICLE PHYSICS. Cambridge University Press; 2017. Available from: `http://www.cambridge.org/academic/subjects/physics/particle-physics-and-nuclear-physics/modern-elementary-particle-physics-explaining-and-extending-standard-model-2nd-ed`
`format=AR&isbn=9781316730805`.

[8] Jönsson L. Lectures in Particle Physics;. `http://www.hep.lu.se/staff/jonsson/fys023/fys023_2012.pdf` [Accessed: 20/4/2019].

[9] Richert TOH. $\Lambda/\mathrm{K}^0_\mathrm{s}$ associated with a jet in central Pb-Pb collisions at $\sqrt{s_{\mathrm{NN}}} = 2.76$ TeV measured with the ALICE detector. Lund U.; 2016-05-16.

[10] Griffiths D. Introduction to elementary particles; 2008.

[11] Chaudhuri AK. A short course on Relativistic Heavy Ion Collisions. IOPP; 2014.

[12] Vislavicius V. Identified Hadron Production as a Function of Event Multiplicity and Transverse Spherocity in pp Collisions at s = 7 and 13 TeV with the ALICE Detector; 2018. Defence details Date: 2018-03-23 Time: 13:00 Place: Rydberg lecture hall, Department of Physics, Sölvegatan 14A, Lund External reviewer(s) Name: Hemmick, Thomas Title: Professor Affiliation: Department of Physics and Astronomy, Stony Brook University, Stony Brook, NY, USA —.

[13] Pasechnik R, Šumbera M. Phenomenological Review on Quark–Gluon Plasma: Concepts vs. Observations. Universe. 2017;3(1):7.

[14] Braun-Munzinger P, Stachel J. The quest for the quark-gluon plasma. Nature. 2007;448:302–309.

[15] Abelev BB, et al. Production of charged pions, kaons and protons at large transverse momenta in pp and Pb–Pb collisions at $\sqrt{s_{\mathrm{NN}}}$ =2.76 TeV. Phys Lett. 2014;B736:196–207.

[16] Ohlson A. Recent results on two-particle correlations in ALICE. J Phys Conf Ser. 2016;668(1):012074.

[17] Aamodt K, et al. Harmonic decomposition of two-particle angular correlations in Pb-Pb collisions at $\sqrt{s_{NN}} = 2.76$ TeV. Phys Lett. 2012;B708:249–264.

[18] Rafelski J. Extreme States of Nuclear Matter - 1980. 1981;p. 282–324. [Reprint: Eur. Phys. J.A51,no.9,115(2015)].

[19] Koch P, Müller B, Rafelski J. From strangeness enhancement to quark–gluon plasma discovery. Int J Mod Phys. 2017;A32(31):1730024.

[20] Torrieri G. Phenomenology of Strangeness enhancement in heavy ion collisions. J Phys. 2009;G36:064007.

[21] Abelev B, et al. Long-range angular correlations on the near and away side in p-Pb collisions at $\sqrt{s_{NN}} = 5.02$ TeV. Phys Lett. 2013;B719:29–41.

[22] Aaboud M, et al. Measurements of long-range azimuthal anisotropies and associated Fourier coefficients for pp collisions at $\sqrt{s} = 5.02$ and 13 TeV and p+Pb collisions at $\sqrt{s_{\mathrm{NN}}} = 5.02$ TeV with the ATLAS detector. Phys Rev. 2017;C96(2):024908.

[23] Khachatryan V, et al. Measurement of long-range near-side two-particle angular correlations in pp collisions at $\sqrt{s}$ =13 TeV. Phys Rev Lett. 2016;116(17):172302.

[24] Adam J, et al. Enhanced production of multi-strange hadrons in high-multiplicity proton-proton collisions. Nature Phys. 2017;13:535–539.

[25] Sjostrand T. PYTHIA 8 Status Report. In: Proceedings, HERA and the LHC Workshop Series on the implications of HERA for LHC physics: 2006-2008; 2008. p. 726–732.

[26] Nassirpour A. Production of Mesons as a Function of Multiplicity Spherocity; 2017. Student Paper.

[27] Bierlich C, Gustafson G, Lönnblad L. A shoving model for collectivity in hadronic collisions. 2016;.

[28] Bierlich C. Microscopic collectivity: The ridge and strangeness enhancement from string–string interactions. Nucl Phys. 2019;A982:499–502.

[29] Bierlich C. Rope Hadronization and Strange Particle Production. EPJ Web Conf. 2018;171:14003.

[30] CERN. The Large Hadron Collider;. `https://home.cern/science/accelerators/large-hadron-collider` [Accessed: 7/5/2019].

[31] Barletta W, Battaglia M, Klute M, Mangano M, Prestemon S, Rossi L, et al. Working Group Report: Hadron Colliders. In: Proceedings, 2013 Community Summer Study on the Future of U.S. Particle Physics: Snowmass on the Mississippi (CSS2013): Minneapolis, MN, USA, July 29-August 6, 2013; 2013. Available from: `http://www.slac.stanford.edu/econf/C1307292/docs/AcceleratorCapabilities/Hadron-30.pdf`.

[32] ATLAS Experiment C. About the ATLAS Experiment;. `https://atlas.cern/discover/about` [Accessed: 7/5/2019].

[33] CERN. CMS;. `https://home.cern/science/experiments/cms` [Accessed: 7/5/2019].

[34] LHCb. LHCb - Large Hadron Collider beauty experiment;. `http://lhcb-public.web.cern.ch/lhcb-public/` [Accessed: 7/5/2019].

[35] Aamodt K, et al. The ALICE experiment at the CERN LHC. JINST. 2008;3:S08002.

[36] Abelev BB, et al. Performance of the ALICE Experiment at the CERN LHC. Int J Mod Phys. 2014;A29:1430044.

[37] Alme J, et al. The ALICE TPC, a large 3-dimensional tracking device with fast readout for ultra-high multiplicity events. Nucl Instrum Meth. 2010;A622:316–367.

[38] Bryngemark L. Charged pion identification at high pT in ALICE using TPC dE/dx. In: 6th International Workshop on High-pT physics at LHC (HPT 2011) Utrecht, The Netherlands, April 4-7, 2011; 2011. .

[39] Abbas E, et al. Performance of the ALICE VZERO system. JINST. 2013;8:P10016.

[40] Collaboration A. Alice events from first LHC Beams;. `http://aliceinfo.cern.ch/Public/en/Chapter1/Events-en.html` [Accessed: 7/5/2019].

[41] Aliroot. Welcome to the home page of the ALICE Off-line Project;. `http://alice-offline.web.cern.ch/` [Accessed: 20/3/2019].

[42] Antcheva I, et al. ROOT: A C++ framework for petabyte data storage, statistical analysis and visualization. Comput Phys Commun. 2009;180:2499–2512.

[43] Torbjörn Sjöstrand CB. Rope Hadronization;. `http://home.thep.lu.se/~torbjorn/pythia82html/RopeHadronization.html#section1` [Accessed: 21/3/2019].

[44] Ortiz Velasquez A, Christiansen P, Cuautle Flores E, Maldonado Cervantes I, Paić G. Color Reconnection and Flowlike Patterns in *pp* Collisions. Phys Rev Lett. 2013;111(4):042001.